Study of Magnetic Features of $Nd_2Fe_{14}B$ through the Spin Reorientation Transition by Magnetic Force Microscopy

by

Muhammad Saleem

M.Sc., King Fahd University of Petroleum and Minerals, 2012

A THESIS SUBMITTED IN PARTIAL FULFILLMENT
OF THE REQUIREMENTS FOR THE DEGREE OF

Master of Science

in

THE FACULTY OF GRADUATE AND POSTDOCTORAL STUDIES
(Physics)

The University of British Columbia
(Vancouver)

April 2017

Abstract

$Nd_2Fe_{14}B$ is one of the high performance permanent magnets that has appeared as an appealing compound for commercial applications. The understanding of its macroscopic magnetic properties through the study of its magnetic domain structures has received great attention. In this study, we use magnetic force microscopy (MFM) to image the magnetic features as a function of temperature through the spin-reorientation transition temperature ($T_{SR} \sim 135$ K) of a $Nd_2Fe_{14}B$ single crystal. We observe a pronounced change in the anisotropy of the magnetic features upon cooling from 170 K to 100 K. Our autocorrelation analysis of the MFM images reveals an increase in the four-fold component of the anisotropy below T_{SR}. The magnetic feature size is estimated from the two-fold and four-fold components and found to be between 4.5 μm and 6 μm below T_{SR}. We observe an average magnetic feature size around 5 μm above the spin reorientation transition. The complexity in the geometry of magnetic features is studied from the fractal dimension (FD) analysis. Higher values of FD below T_{SR} indicate that the magnetic features possess more rugged boundaries. Average values of FD increase from 1.17 ± 0.05 for $T > T_{SR}$ to 1.29 ± 0.04 for $T < T_{SR}$.

Preface

The magnetic force microscopy (MFM) experiment was carried out in Hoffman lab in Harvard University by M. Huefner. The sample used in the experiment was provided by R. Prozorov and P. C. Canfield from Iowa State University. Xiaoyu Liu contributed in developing MATLAB code for accessing the MFM data. The data was analyzed and interpreted by the author and Jason Hoffman. The main results of this thesis will be published on arXiv and in suitable peer-reviewed journals.

Table of Contents

List of Tables

List of Figures

Acknowledgments

I would like to express my sincere gratitude to my research supervisor Prof. Jennifer Hoffman for giving me the opportunity to work in her group. I am very grateful for the moral and financial support she provided to complete my master's degree. I would like to acknowledge with much appreciation her guidance, encouragement, and kindness during my studies.

I am really thankful to my academic supervisor Prof. Robert Kiefl for reading my thesis and for his moral support.

A special gratitude to Dr. Jason Hoffman for his availability and fruitful discussion over analysis and results. I am thankful to him for helping me in MATLAB and reviewing my thesis draft. I really appreciate the motivation that you gave me during my research.

In addition, I would like to say "thank you" to all of the staff and faculty members in the department of physics and astronomy. I am also thankful to all my friends for being with me and having many useful discussions on course material and research related activities.

Finally, I would like to thank my family for their best wishes, unlimited support and encouragement. I wish to dedicate this thesis to my both beloved sons Moaz S. Khan and Hassan S. Khan.

Chapter 1

Introduction

1.1 Background

Permanent magnets are important due to applications in turbines, electronics, electric motors, automobile engines, hard drives, nanoscale devices, medical applications, research tools/equipments and many more [1–7]. These applications can be optimized by developing materials with high coercivity, high remanence, large energy product $(BH)_{max}$, and an almost rectangular hysteresis loop. Figure 1.1 shows the chronological development of energy product of magnets in the 20^{th} century. Nd-Fe-B type magnets show the highest energy products compared to other permanent magnets.

Most of the commercially available permanent magnets are rare earth transition metals compounds. In these materials, the rare earth elements provide most of the magneto-crystalline anisotropy responsible for the coercivity, while magnetization emerges because of the transition metal sublattice [9]. $Nd_2Fe_{14}B$ has become an effective candidate due to its low cost, its high energy product (50 MGOe) [10], and its high saturation magnetization (1.6 T) [11]. It is also suitable for light and small designs due to its low specific gravity. Thus, $Nd_2Fe_{14}B$ has become the most widely used high performance permanent magnet.

$Nd_2Fe_{14}B$ like other permanent magnets possess magnetic domains. Magnetic domains describe small regions of uniform magnetization. Generally,

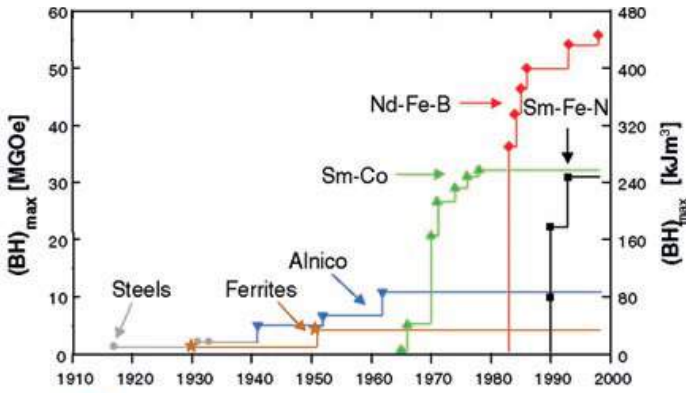

Figure 1.1: Development in the energy density $(BH)_{max}$ of hard magnetic materials in the 20^{th} century (adapted from Ref.[8]). Nd-Fe-B type magnets dominate other type of magnetic compounds due to highest energy product.

the direction of magnetization varies from domain to domain. An external magnetic field is applied to align them, as a result, magnetic materials give non-zero bulk magnetization. The domains are separated by small regions are called domain walls. Domain walls are the transition region that represent the continuous change in spin direction. The deep understanding of magnetic microstructures enable us to predict the magnetic behavior of hard magnets such as $Nd_2Fe_{14}B$. Further, magnetic microstructure of hard magnets is of interest for nanoscale devices. In micromagnetic models the domain wall energy density 'γ' is a fundamental parameter, knowledge of which is very important for the application of micromagnetics [12]. In addition, the study of magnetic domains is useful for understanding and determining domain wall energy, magnetic behavior and thermal remagnetization [13]. Therefore, a detailed understanding and complete knowledge of magnetic domains and intrinsic magnetic properties of $Nd_2Fe_{14}B$ magnets are worth studying.

$Nd_2Fe_{14}B$ has a Curie temperature $T_c = 565$ K and shows a spin reorientation transition at $T_{SR} = 135$ K [9]. Above T_{SR}, the easy magnetization direction is the c-axis. At T $\leq T_{SR}$, the easy magnetization direction cants away from c-axis and changes into four equivalent magnetization axes in

{110} planes, forming an easy-cone-like magnetization [14, 15]. Magnetic microstructures change significantly from temperature above T_{SR} to below T_{SR}.

Several different experimental techniques, including magneto-optic Kerr effect, transmission electron microscopy, scanning electron microscopy, and magnetic force microscopy (MFM) have been used to investigate the magnetic domain properties of $Nd_2Fe_{14}B$ [16–25]. At room temperature, the magnetic domains form star-like patterns, which evolve into larger rectangular shape domain features below T_{SR} [16]. Smaller domains, with a characteristic length scale of 0.02 μm – 0.5 μm are observed well-above T_{SR} [24–29], while at 4 K, domains with size of 2 μm – 5 μm are observed [16]. At 200 K, magnetic features at nano-meter length scale (from 6 nm to 40 nm) in the bulk with domain wall thickness of 6 nm has been reported using small-angle neutron scattering technique [26]. Furthermore, magnetic domain of size 20 nm and 25 nm have also been reported by Huang, *et al.* [25] and Al-Khafaji, *et al.* [24], respectively, using MFM measurements at room temperature.

1.2 Motivation

Although most commercial applications of $Nd_2Fe_{14}B$ magnets are well above the T_{SR}, the microscopic study of its domain features as a function of temperature crossing through the T_{SR} is important for understanding the magnetic phase transition. In previous studies, not much attention was paid to the study of magnetic features through the spin reorientation transition.

In this work, we track the magnetic features of a $Nd_2Fe_{14}B$ single crystal through T_{SR} using magnetic force microscopy (MFM). MFM has established itself as a phenomenal tool to gain spatially resolved information about magnetic structures with high resolution [30, 31]. In our analysis, we explore two main characteristics of the magnetic features of $Nd_2Fe_{14}B$ in the temperature range 170 K to 100 K.

1. We investigate the typical length scale of magnetic features in both temperature regimes i.e., above and below T_{SR}.

2. We explore the fractal dimension (FD) associated with the magnetic features below and above T_{SR}.

1.3 Brief description of chapters

Chapter two

This chapter summarizes the fundamental properties of $Nd_2Fe_{14}B$ such as crystal structure, magnetic anisotropy, and the spin reorientation transition. These properties are discussed in light of previous studies. A review of the literature on $Nd_2Fe_{14}B$ is also provided, with an emphasis on the experimental studies of magnetic domain structure.

Chapter three

In this chapter, we discuss fundamentals of the MFM, including the working principle and its different operational modes. The experimental approach carried out to obtain the MFM images is also discussed.

Chapter four

In this chapter we describe the analysis of the MFM images. We estimate the length scale associated with magnetic domain features. We calculate the two-dimensional autocorrelation of MFM images. The autocorrelated images possess two-fold, as well as, four-fold anisotropies. We track the two-fold and four-fold components of the anisotropies as a function of different radii. The radii represent the average length scale associated with magnetic features.

Chapter five

This chapter is on the fractal dimension (FD) analysis of magnetic features. We introduce the fundamentals of fractals in general, and the various methods that have been developed to study the fractals. A very brief description of prevalent methods of fractal analysis is provided. The area-perimeter

method is discussed and used to obtain the FD as a function of temperature.

Chapter six

In this last chapter of the thesis, conclusions of our analysis are presented. Future work is also proposed.

Chapter 2

Fundamentals and Literature Review

2.1 Fundamentals

2.1.1 Crystal structure

Shortly after its discovery, the crystal structure of $Nd_2Fe_{14}B$ was studied by Herbst, *et al.* [32], Givord, *et al.* [33] and Shoemaker, *et al.* [34] independently. The crystal structure is tetragonal, with lattice constants $a = 8.80$ Å and $c = 12.20$ Å . Each $Nd_2Fe_{14}B$ unit cell is composed of 68 atoms with 56 Fe, 8 Nd and 4 B atoms arranged in an eight-layer structure, as shown in Fig. 2.1. Every Nd and B atom is bonded to 4 Fe atoms in the mirror planes at $z = 0$ and $z = 1/2$. In between these planes, the remaining Fe atoms construct a hexagonal net. Therefore, a unit cell of $Nd_2Fe_{14}B$ shows sheets of Fe, Nd and B atoms separated by hexagonal iron nets. The Fe-Fe separation is less than Fe-Nd separation, while all the pairs in the unit cell are separated by less than 4 Å [9]. There are six different sites for Fe atoms, two different sites for Nd atoms and only one site for B atoms as shown by the table in Fig. 2.1.

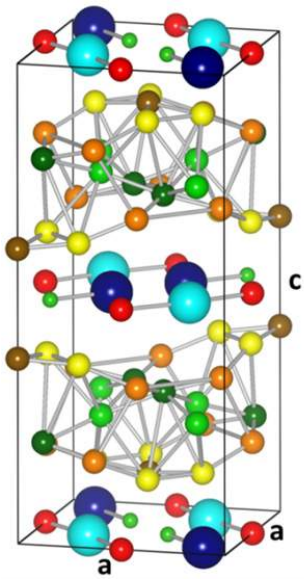

Atom	x	y	z
Nd(4f)	0.268	0.268	0.0
Nd(4g)	0.140	-0.140	0.0
Fe(16k_1)	0.223	0.567	0.127
Fe(16k_2)	0.037	0.360	0.176
Fe(8j_1)	0.098	0.098	0.204
Fe(8j_2)	0.317	0.317	0.246
Fe(4e)	0.5	0.5	0.114
Fe(4c)	0.0	0.5	0.0
B(4g)	0.371	-0.371	0.0

Figure 2.1: Tetragonal unit cell of $Nd_2Fe_{14}B$ with lattice constants a = 8.80 Å and c = 12.20 Å . The c-axis is elongated to emphasize the puckering of hexagonal iron net. The table indicates the atomic sites, occupancies, and coordinates (x,y,z) of constituent atoms. This figure is adapted from Ref.[35].

2.1.2 Magnetic anisotropy

Magnetic anisotropy is the characteristic of magnetic materials (ferromagnetic and ferrimagnetic) when magnetic moments are aligned to any energetically favorable crystallographic axis to achieve the minimum energy. Magnetic anisotropy or magneto-crystalline anisotropy describes the directional dependence of magnetic properties. The primarily origin of magneto-crystalline anisotropy is the spin-orbit interaction.

For magnetic materials, there are two magnetization directions: the easy-magnetization direction and the hard-magnetization direction. The easy magnetization direction is obtained through a small applied field to achieve the saturation magnetization inside the crystal. On the other hand, the hard magnetization axis represents that direction in space where large magnetic

field is required to achieve saturation magnetization. Thus, one would need a strong magnetic field to achieve the saturation magnetization along hard-axis compared to easy-axis. The magnetization curves of $Nd_2Fe_{14}B$ along easy- and hard-axis are shown in Fig. 2.2.

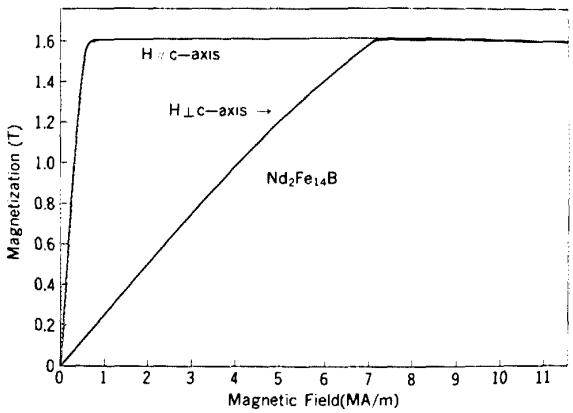

Figure 2.2: Magnetization along easy- and hard-axis in $Nd_2Fe_{14}B$ single crystal measured at room temperature (adapted from Ref.[11]). Large magnetic field up to 7 MA/m is required to achieve the magnetization perpendicular to c-axis i.e., along hard-axis, while magnetic field less than 1 MA/m is sufficient to magnetized $Nd_2Fe_{14}B$ single crystal along c-axis.

$Nd_2Fe_{14}B$ has uniaxial magnetic anisotropy i.e., easy-axis is aligned with tetragonal c-axis above T_{SR}. In tetragonal symmetry, the magneto-crystalline anisotropy energy can be approximated by:

$$E = E_0 + K_1 \sin^2\theta + K_2 \sin^4\theta + K_3 \sin^4\theta \cos 4\phi, \tag{2.1}$$

where E_0 is constant, θ is the angle between the magnetization vector and the c-axis, and ϕ is the angle between the magnetization vector and the a-axis. These angles determine the orientation of the magnetization vector with respect to crystallographic axes. K_1, K_2 and K_3 are anisotropy constants. The anisotropy constants have no direct correlation with the physical origin of magnetic anisotropy, rather they reflect only magnetic anisotropy phenomenologically [36]. However, these constants are strongly temperature

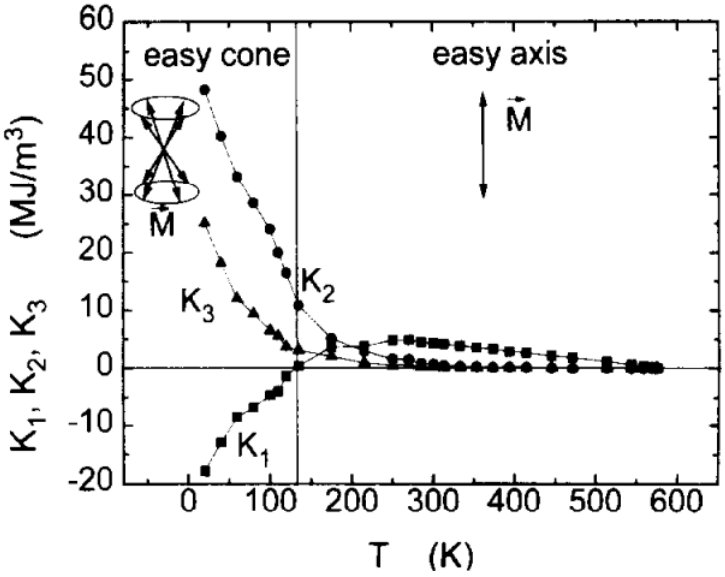

Figure 2.3: Temperature dependence of magnetic anisotropy constants of $Nd_2Fe_{14}B$ (adapted from Ref.[16]). The spin reorientation takes place at 135 K, where K_1 becomes negative and K_2 and K_3 increase abruptly.

dependent and have been estimated experimentally as a function of temperature [37]. The temperature dependent behavior of anisotropy constants for $Nd_2Fe_{14}B$ are shown in Fig. 2.3. With increasing temperature from 4.2 K, K_1 increases from negative to positive. On the other hand, at 4.2 K, both K_2 and K_3 are positive and decrease with increasing temperature. K_2 remains positive, while K_3 becomes negligibly small above T_{SR}.

The anisotropy constants K_1 and K_2 are dominant and basal plane anisotropy constant K_3 is small. The energy minimization can be derived from the conditions $\frac{\partial E}{\partial \theta} = 0$ and $\frac{\partial^2 E}{\partial \theta^2} > 0$. Depending on values of K_1 and K_2, three cases namely, easy-axis, easy-plane, and easy-cone can be considered. Figure 2.4 illustrates the easy-axis, easy-cone, and easy-plane magnetization in tetragonal symmetry.

i. For $K_1 \geq 0$ and $K_1 + K_2 > 0$, then $\theta = 0°$ or $180°$. This shows the preferred magnetization direction along c-axis.

ii. For $K_1 < 0$ and $K_1 + 2K_2 < 0$ or $K_1 > 0$ and $K_1 + K_2 < 0$, then $\theta = 90°$. This is an easy-plane where the preferred magnetization direction is perpendicular to c-axis.

iii. For $K_1 < 0$ and $K_1 + 2K_2 > 0$, then $\sin^2\theta = -\frac{K_1}{2K_2}$. This indicates that the preferred magnetization direction will be some where between easy-axis and easy-plane in the space. This is the situation when there will be four equivalent preferred axes form an easy-cone.

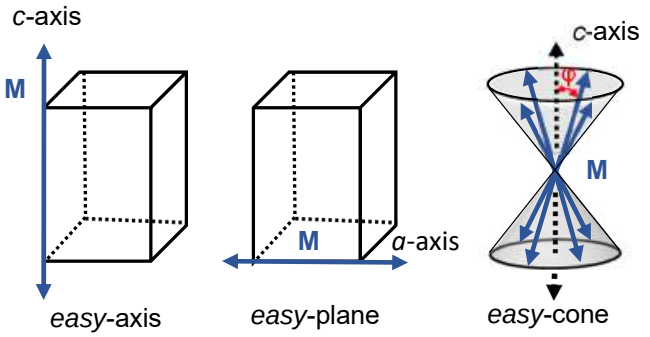

Figure 2.4: Three different easy magnetization directions for tetragonal symmetry. **M** is the net magnetization aligned to a preferred direction. Easy-axis representation is when **M** is aligned along the c-axis, easy-plane representation is when **M** is in the basal plane, and easy-cone representation is when **M** is on the surface of cone.

2.1.3 Spin reorientation transition

Generally the application of three factors (temperature, magnetic field, and external pressure) change the direction of easy-axis of magnetization from one crystal axis to any other axis. The phenomena of net magnetization deflection away from one crystallographic axis at high temperature to another at low temperature is called the spin reorientation transition (SRT). The temperature at which the SRT takes place is known as the spin reorientation transition temperature (T_{SR}). The occurrence of SRT destroys

the uniaxial anisotropy and worsen the magnetic performance of permanent magnets for technological applications [9].

The SRT can proceed either through first-order (discontinuous) transition or through second-order (continuous) transition. In the first-order transition i.e., easy-axis to easy-plane, the easy-axis of magnetization changes rapidly from axial to planar (in basal plane) with decreasing temperature. This transition is not mediated by conical arrangement. Among $R_2Fe_{14}B$ compounds, $Er_2Fe_{14}B$, $Tm_2Fe_{14}B$, and $Yb_2Fe_{14}B$ have shown the first-order SRT [9]. In these compounds, Fe and R (= Er, Tm, Yb) sublattices have temperature induced competition of magnetic moments alignment. Intermetallic compounds such as $TbFe_{11}Ti$, $DyFe_{11}Ti$, and $NdCo_5$ have shown both types i.e., first- and second-order transitions.

$Nd_2Fe_{14}B$ has second-order SRT, where easy-axis magnetization changes to easy-cone magnetization. Above T_{SR} ($T = 135$ K), Fe and Nd magnetic moments are ferrimagnetically coupled and have collinear alignment with

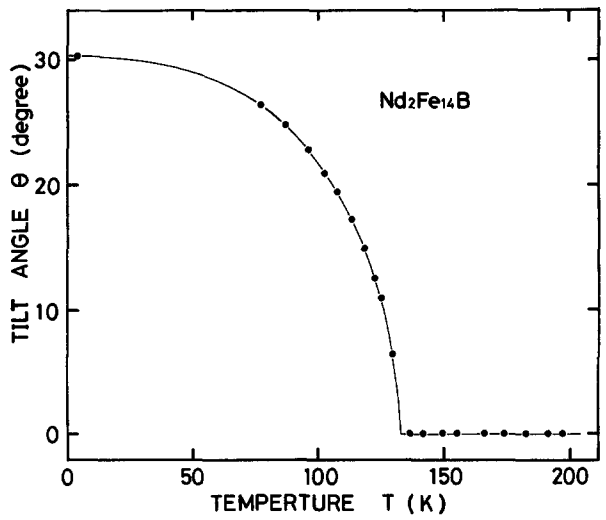

Figure 2.5: Tilt angle as a function of temperature in single crystal of $Nd_2Fe_{14}B$ (adapted from Ref.[14]). The canting angle is zero for $T > T_{SR}$ and increases for T $\leq T_{SR}$. The maximum canting angle is about 30° at 4.2 K.

c-axis. Therefore, easy-axis magnetization remains along [001] direction. At T_{SR}, easy-axis magnetization changes into four easy magnetization directions (in {110} planes) on the surface of a cone with some canting angle. The canting angle is temperature sensitive, and increases from 0° (uniaxial) to 30° at 4.2 K [14, 38]. Figure 2.5 shows the increase in canting angle with temperature.

There are several studies carried out to understand the origin of SRT in $Nd_2Fe_{14}B$. It is considered that the strong interplay between crystal field and Fe-Nd exchange interaction causes the SRT [15, 39]. Generally, crystal field and exchange interaction are temperature dependent. It was revealed that the reorientation of the magnetization towards the c-axis at higher temperature is due to the relative decrease of crystal field interaction with respect to exchange interaction, which favors a collinear arrangement of Nd and Fe moments [15, 40]. Some experimental findings have shown the existence of non-collinear arrangement of both Fe and Nd magnetic moments throughout the spin reorientation transition [41–43]. These findings indicated that Nd and Fe canting angles reach up to 58° and 27°, respectively, at 4.2 K.

2.2 Literature review

A wide-variety of experimental techniques have been used to investigate the magnetic domains of $Nd_2Fe_{14}B$. The majority of studies were conducted at room temperature (RT) or well above the T_{SR}. Some studies have also been conducted well below T_{SR}. The domains of different types, geometry, and different orientations depend on several factors. For instance, the domains observed in prismatic plane [100] (plane parallel to c-axis) are completely different than domains observed in the basal plane [001] (plane perpendicular to c-axis). Domain features are distinct and vary significantly from $T > T_{SR}$ to $T < T_{SR}$.

Room temperature magneto-optical Kerr effect (MOKE) measurements revealed star-like domains in the basal plane, while stripe-like domains were observed in the prismatic plane of $Nd_2Fe_{14}B$ single crystals [16]. Figure 2.6 shows the temperature dependent domain evolution in basal and prismatic

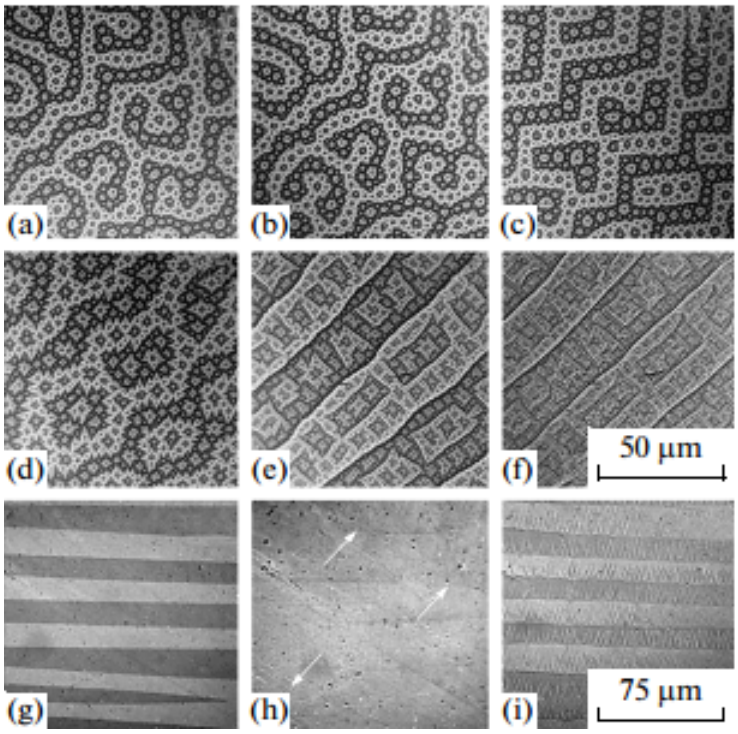

Figure 2.6: MOKE images of single crystal of $Nd_2Fe_{14}B$ (adapted from Ref.[18]). Transformation of domain structures on basal (a – f) and prismatic (g – i) planes as a function of temperature. $T =$ (a) 285, (b) 200, (c) 165, (d) 118, (e) 113, (f) 20, (g) 285, (h) 135, and (i) 20 K. Different types of domains are present on different planes of observation. Star-like domains exist on basal plane and transform into rectangular-like domains below T_{SR}. Stripe-like domains emerge on prismatic plane.

planes of $Nd_2Fe_{14}B$ single crystal. In the prismatic plane, stripe domains, with width 63 μm were observed above T_{SR}. Similar type of domain structure (53 μm) with immediate appearance of closure domains of width 2 μm – 5 μm were observed below T_{SR} [16]. On the other hand, star-like domains in the basal plane change into a new type of rectangular domain upon decreasing the sample temperature below T_{SR}. A domain size of about 5 μm in the basal plane was reported below T_{SR} [17]. The emergence of new type of domains is apparent on all planes of observation and are the consequence

of change in the preferred orientation of domain walls [16–18].

Scanning electron microscopy (SEM) [19–21] and transmission electron microscopy (TEM) [20, 22] revealed magnetic domains in maze-like pattern with spike reversed domains having opposite polarity on the basal plane of $Nd_2Fe_{14}B$ single crystals. Maze-like pattern observed by SEM and TEM are shown in Fig. 2.7. The spike domains are the surface domains, while

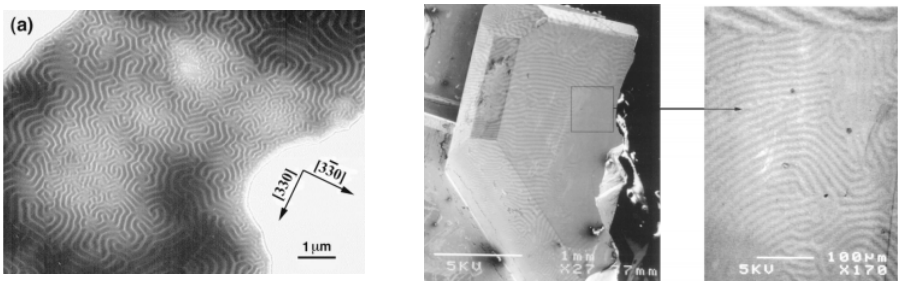

(a) TEM image adapted from Ref.[20]. **(b)** SEM image adapted from Ref.[21].

Figure 2.7: Both TEM and SEM images reveal maze-like pattern of magnetic domains of a (001) crystal of $Nd_2Fe_{14}B$.

the maze domains extend into the bulk. The stray field at the surface was also viewed three-dimensionally forming the hillocks separated by troughs [19, 21], which revealed that the origin of stray field at the sample surface is maze domain pattern. Apart from the $Nd_2Fe_{14}B$ phase, magnetic domains of Nd-Fe-B alloys have also been investigated. Scanning transmission X-ray microscopy study of 50 nm – 150 nm thin *c*-plane sample of Nd-Fe-B sintered magnet showed maze-like pattern domains configuration of width 150 nm – 200 nm [22]. Similar domains of width about 150 nm with domain wall of thickness 3 nm in Nd-Fe-B alloy were reported by Mishra, *et al.*, [44]. A Bitter pattern technique reported the same type of domains [28] i.e., maze pattern and spike reversed domains on the basal plane of thermally demagnetized sample. However, observed domains were found to be 3 μm – 6 μm wide. Interestingly, the very same Nd-Fe-B sample revealed domains of width 1 μm – 3 μm from SEM study and fine magnetic domains with wide range of width 20 nm – 250 nm from MFM measurements [28]. These discrepancies in the domain size of same surface clearly evidence the limited

resolution of Bitter and SEM compared to MFM.

Figure 2.8: Scanning transmission X-ray microscopy image of 20 μm $\times$ 20 μm Nd-Fe-B sintered magnet with thickness 50 – 150 nm. Maze-like domain patterns are clearly observed. This figure is adapted from Ref. [22].

MFM study of thin Nd-Fe-B films composed of small rectangular grains of 1 μm – 2 μm showed the stripe domains of width of 100 nm – 300 nm [23]. Al-Khafaji, *et al.* [24] reported the magnetic features on the order of 25 nm in a rick-rack domain pattern in the basal plane of $Nd_2Fe_{14}B$ single crystal. It was also noticed that the small tip-sample separation enhances the image resolution and fine scale magnetic features can be seen. Recently, another MFM study showed star-like magnetic domains at RT as a result of complex network of elongated domains [25]. Magnetic domains of width 20 nm with domain wall of thickness about 2 nm were reported. The feature size (domain wall thickness) of 2 nm is much less than MFM resolution, and suggests the possibility of a tip artifact. In MFM studies, tip-induced artifacts should not be ruled out, as they can cause a misinterpretation of the domain structure [45].

The domain structure in the basal plane of a $Nd_2Fe_{14}B$ single crystal was also studied by small angle neutron scattering [26]. The magnetic domains

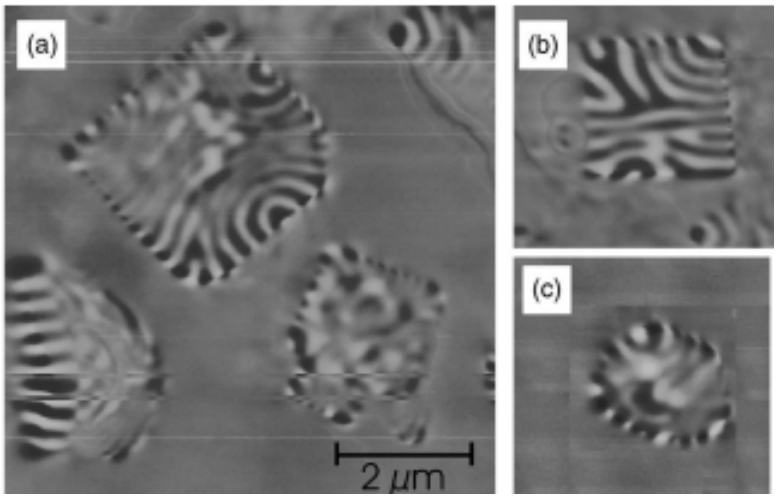

Figure 2.9: MFM image of Nd-Fe-B film. Small 1 μm – 2 μm grains of $Nd_2Fe_{14}B$ show magnetic domains with domain size about 150 nm. This figure is adapted from Ref. [23].

of length scales 6 nm – 40 nm were found and are in comparable range to length scale observed by MFM. Furthermore, this study also showed that high temperature (T = 200 K) magnetic features are smoother than magnetic features below T_{SR} at 20 K.

Table 2.1 summarizes the magnetic feature sizes observed by different experimental techniques. Domains with characteristic length scale of 0.02 μm – 0.5 μm appear above T_{SR}. Domain with larger length scale (2 μm – 5 μm) are observed below T_{SR} (4.2 K). These experimental results indicate the discrepancies in domain size and observed domain structure. For instance, star-like magnetic features were not observed in TEM and SEM images above T_{SR}, unlike MOKE and MFM images. The difference in domain features might have the following reasons:

i. different surface sensitivity of the measurement technique.

ii. different spatial resolution of the measurement technique.

iii. plane of observation of the sample.

iv. temperature and thickness of the sample.

v. presence or absence of applied magnetic field.

Table 2.1: Summary of domain size observed by different measurement techniques.

T(K)	Measurement Technique	Technique Resolution	Domain Size	References
RT	MFM	25 nm	25 nm	Al-Khafaji, *et al.* [24]
RT	MFM	–	100 – 300 nm	Neu, *et al.* [23]
RT	MFM	15 nm	20 nm	Huang, *et al.* [25]
RT	MFM	–	20 – 250nm	Szmaja, *et al.* [28]
RT	Bitter pattern	0.5 μm	3 – 6 μm	Szmaja, *et al.* [28]
RT	SEM	0.1 μm	1 – 2 μm	Szmaja, *et al.* [28]
4.2	MOKE	–	2 – 5 μm	Pastushenkov, *et al.* [16]
200	SANS	–	40 nm	Kreyssig, *et al.* [26]

Furthermore, very little attention has been paid to the magnetic features near the spin reorientation transition. Therefore, it is worthwhile to study the magnetic features and associated characteristic length scale of magnetic features through T_{SR}.

Chapter 3

Magnetic Force Microscopy

3.1 Working principle

Magnetic force microscopy (MFM) is a scanning probe techniques that is used to study the surface properties of magnetic samples with submicron resolution. MFM was first introduced in 1987 [46, 47], soon after the invention of the atomic force microscope (AFM) in 1986 by Binnig, *et al.* [48]. MFM has received considerable attention in academic, as well as, in industrial research due to its high resolution and minimal sample preparation requirements. Further, this technique provides the direct observation of magnetic features.

The simple schematic shown in Fig. 3.1 illustrates the working principle of the MFM. It consists of a cantilever, which has a small needle-shaped magnetized tip on its free end. When the cantilever is brought close to the surface of the sample, generally few hundred of nanometers, the tip-sample interaction leads to a change in cantilever resonance frequency. The tip-sample interaction is either attractive or repulsive depending on the direction of tip magnetization and stray field. The amount of deflection is recorded by an optical detector. The cantilever resonance and phase deflections are obtained while scanning the tip in a raster-like pattern over the sample surface and are processed by a computer program to construct the MFM image in real time.

The cantilever and tip are usually made of Si or Si_3N_4. In order to make the Si tip magnetic, the tip is coated with a thin layer of magnetic material e.g., CoPt, NiFe, or CoCr. The cantilever is typically a few hundred microns (200 μm – 300 μm) in length, while a tip up to a few microns (5 μm – 20 μm) in length is generally used. The radius of the end of the tip plays a vital role in the image resolution. Therefore, tips with small apex radii are preferred for high resolution images. Coated tips of apex radii 15 nm – 50 nm are used.

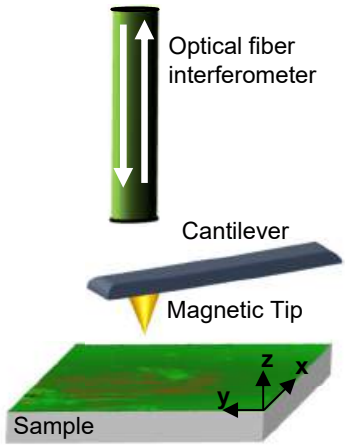

Figure 3.1: A schematic diagram showing the working principle of MFM measurements. A cantilever with magnetic tip is scanned at constant height above the sample surface. The optical interferometer detects the shift in the resonance frequency of the cantilever due to magnetic interaction (constant height mode).

3.2 Tip-sample interaction

The tip-sample surface interaction depends on several parameters that includes tip shape, radius of tip apex, thickness of tip coating, and tip-sample separation. Tip-sample separation is chosen with care during the MFM measurements, because interaction becomes stronger close to the surface. The tip can be remagnetized if the surface stray field is stronger than the

tip coercivity [28, 49], which might cause an artifact in the MFM results. It has also been reported that the type of coated material on the tip (soft or hard tip) and radius of the apex of the tip may produce different magnetic structures [45, 49, 50].

Tip of the MFM acts as a tiny magnet that interacts with the stray field of the sample above the surface. The magnetic interaction i.e., magnetic force on the tip can be calculated by first calculating the magnetic potential energy E and magnetic force $\overrightarrow{F}$ acting on the MFM tip [51]:

$$E = -\mu_0 \int \overrightarrow{M}_{tip} \cdot \overrightarrow{H}_{sample} \mathrm{d}V_{tip} \quad \text{(Joule)} \tag{3.1}$$

$$\overrightarrow{F} = -\overrightarrow{\nabla} E = \mu_0 \int \overrightarrow{\nabla} (\overrightarrow{M}_{tip} \cdot \overrightarrow{H}_{sample}) \mathrm{d}V_{tip} \quad \text{(Newton)} \tag{3.2}$$

where M_{tip} is tip magnetization and H_{sample} is the stray field from the sample. The integration is carried out over the tip volume.

3.3 MFM operational modes

MFM has two modes of operations, the static and the dynamic mode.

3.3.1 Static mode

Static mode is also sometimes called constant or DC mode. In this mode of detection, the force of interaction (repulsive or attractive) between tip and surface causes the cantilever to bend. The force of interaction is measured through the detection of vertical deflection in the cantilever's equilibrium position. According to Hook's law, the magnetic force $|\overrightarrow{F}|$ detected in this mode of operation is [51]:

$$|\overrightarrow{F}| = -c\Delta z, \quad \text{(Newton)} \quad or \quad \Delta z = -\frac{|\overrightarrow{F}|}{c} \tag{3.3}$$

where Δz is the vertical displacement of cantilever as a result of the force and c is the cantilever constant.

3.3.2 Dynamic mode

In the dynamic or AC mode of operation, the cantilever oscillates close to its free resonance frequency f_0 i.e., the resonance frequency when there is no tip-sample interaction. Here, the cantilever is treated as a harmonic oscillator such that the force gradient $\frac{\partial F}{\partial z}$ changes the resonance frequency to [51, 52]

$$f = f_0 \sqrt{1 - \frac{\frac{\partial F}{\partial z}}{c}} \quad \text{(Hz)}. \tag{3.4}$$

For $\frac{\partial F}{\partial z} \ll c$, using a Taylor expansion, the change in resonance frequency is approximated by

$$\Delta f = f - f_0 \approx -\frac{f}{2c} \frac{\partial F}{\partial z} \quad \text{(Hz)}. \tag{3.5}$$

If the tip-sample interaction is attractive, then $\frac{\partial F}{\partial z} > 0$. This leads to a decrease in the resonance frequency. In the case of repulsive interaction ($\frac{\partial F}{\partial z} < 0$), the resonance frequency increases and leads to a positive frequency shift.

3.4 MFM lift-mode

The cantilever deflection may emerge due to the presence of electrostatic, van der Waals, and quantum mechanical forces other than the magnetic force. These forces are distance dependent and are listed with their range of detection in Fig. 3.2. MFM scans may therefore, contain both topographic and magnetic information. If the tip is in close proximity of the surface, where the AFM tapping mode operates, then topographic features will dominate the magnetic contrast. Thus, magnetic features will not be obvious. The topographic features generally result from van der Waals interactions. On the other hand, magnetic forces are long-range forces, which can be sensed at distances much longer than van der Waals. Therefore, the tip is lifted from the surface and scan proceeds at constant height in order to avoid (minimize) the influence of van der Waals forces.

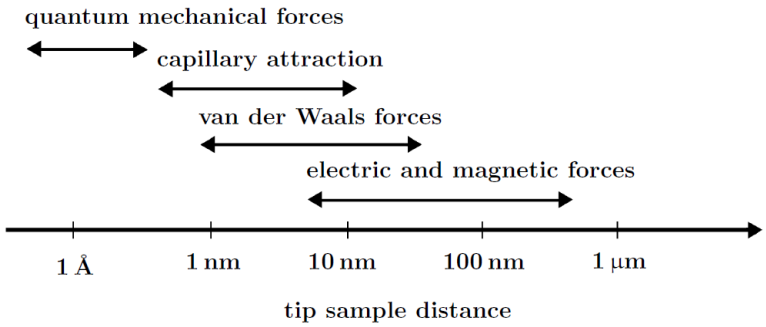

Figure 3.2: Range of detection of different forces that contribute to the tip-sample interaction. The electric and magnetic forces are long range forces and can be sensed up to few hundred of nanometers, which is beyond the detection limit of van der Waals forces. This figure is adapted from Ref.[51].

In constant height mode, dual (two pass) scanning is carried out. The first scan is the topographic scan, where tapping mode with a feedback loop on is operated. The feedback loop adjusts the tip-sample distance and maintains the constant amplitude of cantilever oscillation. In the second scan, the tip is lifted to a constant height and retraces the first scanned profile without feedback loop. The resulting interaction between the MFM tip and surface stray field produces a magnetic field gradient with no dependence on surface topography. A cartoon of lift-mode is shown in Fig. 3.3.

The cantilever frequency shift is detected in three ways: frequency modulation, phase modulation, and amplitude modulation, as shown in Fig. 3.4. In frequency modulation, the shift in cantilever resonance frequency is detected. Phase modulation detects the variations in the phase of the cantilever oscillation relative to the piezo drive frequency, whereas amplitude modulation measures changes in the cantilever oscillation amplitude. Frequency and phase modulation generally produce better results compared to amplitude modulation, with greater ease of use, higher signal-to-noise ratio, and fewer artifacts [55].

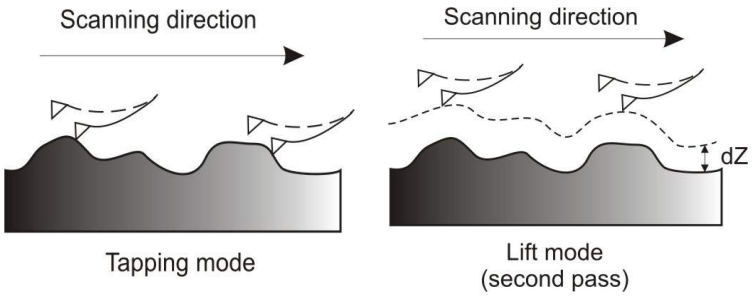

Figure 3.3: Working principle of lift-mode MFM showing two pass scanning. The first scan is done in tapping mode without magnetic information, while magnetic information is recorded during the second pass in lift mode (adapted from Ref.[53]).

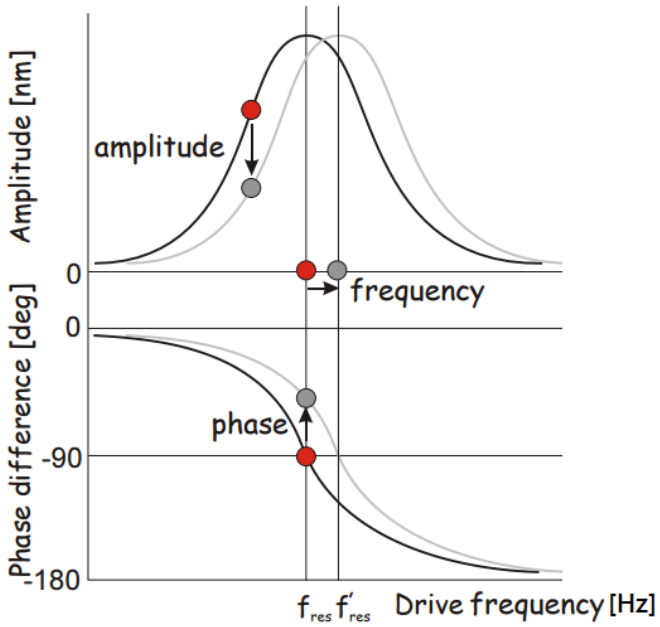

Figure 3.4: The resonance frequency shift of cantilever detected in three different ways as result of changes in magnetic force on the tip (adapted from Ref.[54]).

3.5 Experimental details

The MFM setup used in this experiment is shown in Fig. 3.5. The home built scanning probe setup is located in a vacuum chamber within a Janis flow cryostat. Magnetic features at the sample surface are mapped using a sharp, high-resolution magnetic tip (Team Nanotec MFM) with cobalt alloy coating. The magnetic coating has a coercivity of 950 Oe, with a magnetic moment of approximately 3.75×10^{-14} emu. The tip has in-plane and perpendicular magnetic remanences of 540 emu-cm^{-3} and 160 emu-cm^{-3}, respectively. The tip radius is less than 25 nm, while the length of the tip was greater than 9 μm. The tip has a conical shape with resonance frequency of 75 kHz and force constant c 3.0 N/m.

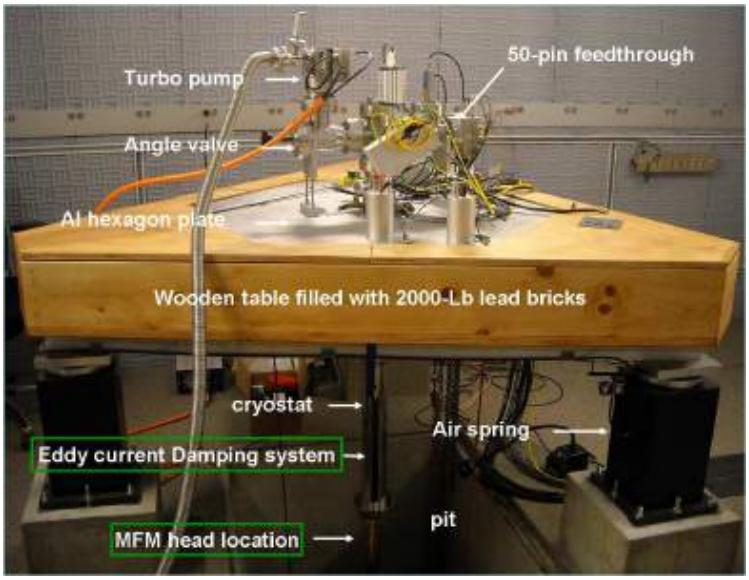

Figure 3.5: The home-built MFM setup situated in Hoffman lab at Harvard university.

A single crystal of $Nd_2Fe_{14}B$ is used. The sample is several millimeter in lateral extent in each direction. The desired surface of study is the basal plan i.e., surface perpendicular to crystallographic c-axis. All the MFM scans were recorded at a base pressure lower than 10^{-7} Torr in the absence

of any external applied magnetic field. Topography of the sample surface is obtained through scanning in contact mode i.e., with very small tip sample separation. Figure 3.6(a) shows a topographic scan measured at room temperature. The topography of the sample is flat with a roughness of several nanometers. However, some particles rising up to several tens of nanometers in height have accumulated on the surface. Another topographic image is taken using a non-magnetic Si-tip, as shown in Fig. 3.6(b). We observe the same kind of topographic structure, indicating no correlation between the topography and the observed magnetic structure. The magnetic features are mapped using lift-up mode at constant height. The measurements are taken with a step size of 5 K while the sample is cooled from 170 K to 100 K.

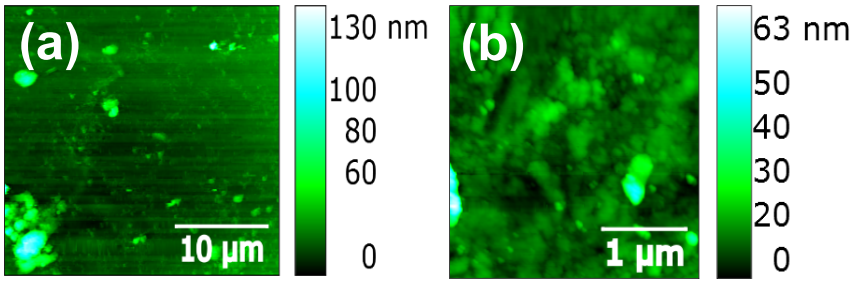

Figure 3.6: Comparison of topography of the sample obtained from two different tips. (a) Shows the topography of the sample (30 μm $\times$ 30 μm) using magnetic tip. (b) Shows the topography of the sample (3 μm $\times$ 3 μm) using the non-magnetic Si-tip.

Chapter 4

Magnetic Feature Analysis

4.1 Magnetic features

Figures 4.1(a) and (c) illustrate a series of 59 μm $\times$ 59 μm MFM images of the $Nd_2Fe_{14}B$ sample taken while cooling from 170 K to 100 K. Above T_{SR}, magnetic features of different length scales over band-like regions are observed. Below T_{SR}, a new type of distorted rectangular magnetic feature appears. There is an onset of magnetic feature rearrangement at T_{SR}, which persists at lower temperatures. We believe that the emergence of distorted rectangular magnetic features below T_{SR} are directly correlated to the change of magnetic phase due to spin reorientation transition. It has been argued that the spin reorientation transition leads the formation of new type of magnetic features [16], because easy axis preferred direction changes from an easy c-axis to four easy magnetization directions in {110} planes.

During the temperature dependent evolution from $T > T_{SR}$ to $T < T_{SR}$, magnetic features show some correlation, which remains in the new magnetic phase. For instance, it can be noticed that some of the magnetic features preserve their location and orientation through the reorientation transition. Continuous modifications in the magnetic features take place due to the temperature dependent change of existing domains and domain walls. The walls of the main magnetic features at high temperature ($T > T_{SR}$) become

elements of the magnetic features of magnetic phase at low temperature ($T < T_{SR}$), while retaining the parallel alignment to the tetragonal c-axis [18]. As a result, we believe that the formation of new type of magnetic features below T_{SR} might be due to mingling of small magnetic features of high temperature ($T > T_{SR}$). Furthermore, the non-vanishing correlation between magnetic features above and below T_{SR} also support this argument.

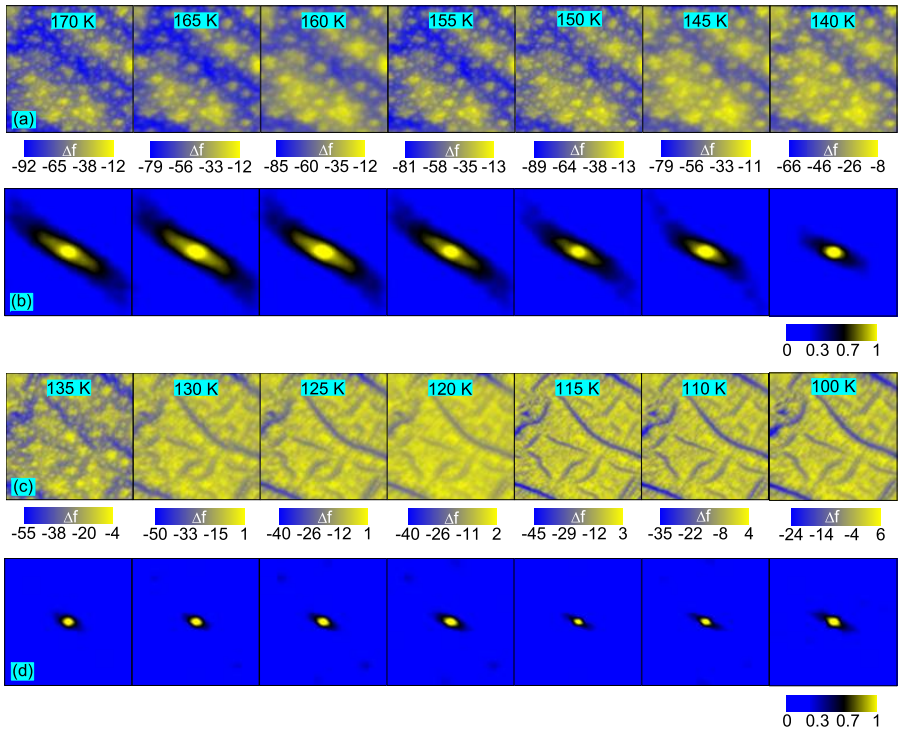

Figure 4.1: (a) and (c) show 59 μm $\times$ 59 μm MFM scans of the same area of the sample at different temperatures below and above T_{SR}. We can see clearly the temperature dependent evolution in magnetic features. (b) and (d) show the normalized 2D autocorrelation (59 μm $\times$ 59 μm) of the MFM-scans shown in part (a) and (c). Autocorrelation of the images is also distinct below and above T_{SR} due to presence of different magnetic features.

4.1.1 Autocorrelation

Correlation is a mathematical method that uses two signals to produce a new signal. If the two input signals are different, then the output signal is called cross-correlation. If the signal is correlated with itself, the resulting signal is called autocorrelation. Correlation is a simple and useful operation sometimes is used to extract the information from images. The autocorrelation of an image helps us in finding the periodic pattern (features) in the image. Autocorrelation is a linear operation because every pixels in autocorrelated result is the linear combination of its neighbors. Furthermore, autocorrelation is also shift-invariant i.e., same operation is performed at every pixel in the image.

For an M×N image, the formula for autocorrelation function $Gii(a,b)$ is [56]:

$$Gii(a,b) = \sum_{x}^{M} \sum_{y}^{N} i(x,y) * i(x-a, y-b), \tag{4.1}$$

where $i(x,y)$ is the image intensity at position (x,y), and a and b represent the distance from the corresponding x and y positions. The formula in equation 4.1 gives theoretical result and are not suitable for limited area calculation. There is an alternative suitable and efficient practical method that uses the fast Fourier transforms using the Weiner-Khinchin theorem [56]:

$$F^{-1}[Gii(a,b)] = S(i) = |F[i(x,y)]|^2, \tag{4.2}$$

where $S(i)$ is the power spectrum of the image and F is the Fourier transform of $i(x,y)$.

4.1.2 Autocorrelation results

The computed two-dimensional autocorrelation of each MFM image is shown in Figs. 4.1(b) and (d). Highly correlated features exist in the center of the autocorrelated images, and the autocorrelation signal diminishes as we go

away from the center of the autocorrelated images. The distinct magnetic features observed in the MFM images are reproduced in the autocorrelated images. A distorted squared type features are observed in the autocorrelated images below T_{SR}, which are absent in the autocorrelated images above T_{SR}, as shown in Fig. 4.2. The features of autocorrelated images seem to possess either two-fold or four-fold anisotropy.

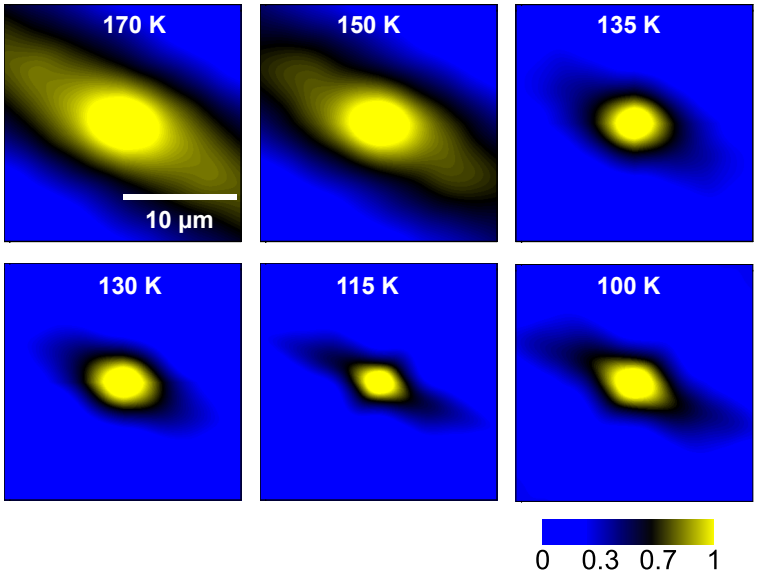

Figure 4.2: Zoomed in (20 μm $\times$ 20 μm) autocorrelated images evidently show the four-fold anisotropy below T_{SR}.

4.2 Analysis approach

4.2.1 Magnetic feature anisotropy

In order to determine the magnetic feature size, we explore the two-fold and four-fold anisotropies in the features of the autocorrelated images. To quantify the anisotropy of magnetic features, we plot the intensity of the autocorrelated images as a function of angle at fixed radii from the center. The radii represent the length scale of magnetic features. Therefore, from

now on, we shall use length scale instead of radius. Figures 4.3(a) and (b) show the autocorrelation amplitude for different length scales at 150 K and 115 K, respectively. We see peaks corresponding to the two-fold and four-fold anisotropies. At 150 K, we only see the two-fold peaks, which become more prominent at larger length scale value. On the other hand, at 115 K, the four-fold peaks emerge with two-fold peaks as the length scale is increased from 2 μm to 6 μm. The appearance of additional four-fold peaks only for low temperatures scans ($T < T_{SR}$) as shown in Fig. 4.2, is attributed to the distorted rectangular magnetic features. To quantify the contribution of the two-fold and four-fold anisotropy components, we fit the autocorrelation intensity Δ using:

$$\Delta = A_0 + A_2 \sin(2\theta + \phi_2) + A_4 \sin(4\theta + \phi_4), \tag{4.3}$$

where A_2 (ϕ_2) and A_4 (ϕ_4) are the amplitudes (phases) corresponding to the two-fold and four-fold anisotropies, respectively. The variation in four-fold coefficient (A_4) with temperature is plotted in Fig. 4.3(c). Temperature dependent behavior of four-fold component displays an abrupt increase around T_{SR}, which persists at lower temperatures.

We use an alternative approach to quantify the changes in the magnetic features. We perform 1D fast Fourier transform (FFT) of the autocorrelation intensity as a function of angle curves exemplified in Figs. 4.3(a) and (b). Figure 4.3(d) shows the four-fold component of the FFT as a function of temperature at several length scales. We find no four-fold contribution above T_{SR}, but there is an abrupt increase in the magnitude of four-fold component below T_{SR}. This temperature dependent behavior of four-fold component is in agreement with analysis in Fig. 4.3(c).

4.3 Magnetic feature size

4.3.1 $T \leq T_{SR}$

Figures 4.4(a) and (b) show the two-fold and four-fold components of the FFT as a function of length scale at different temperatures. Below T_{SR} we

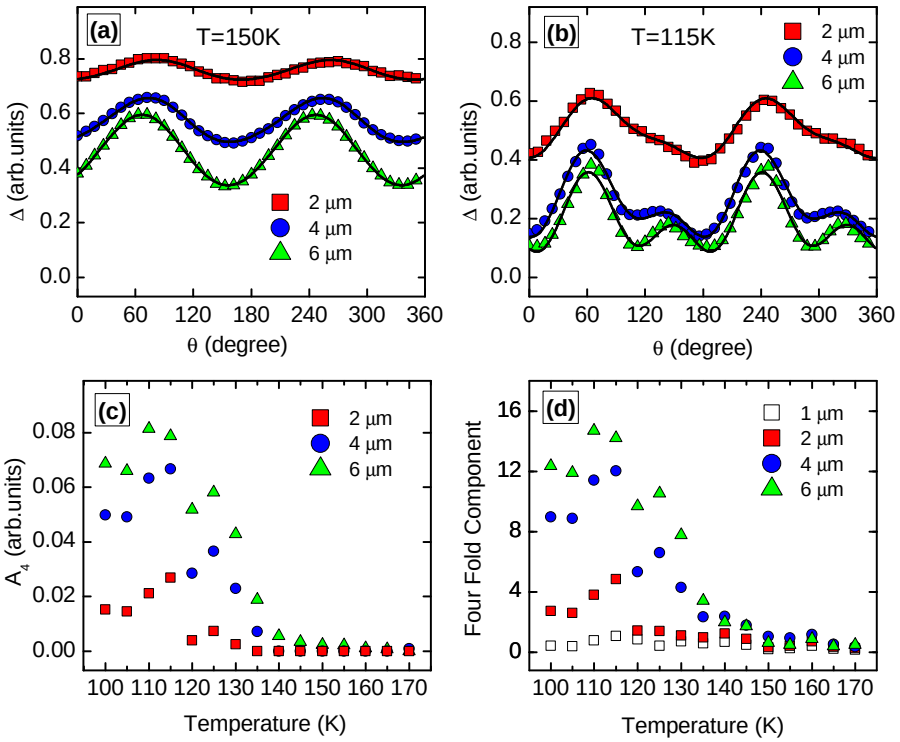

Figure 4.3: (a) and (b) show the autocorrelation intensity as a function of angle at 150 K and 115 K, respectively. Symbols show the intensity for different length scales from Fig. 4.1(b) and (d). The black line is the fitting curve by equation 4.3. (c) Variation in four-fold coefficient A_4 with temperature, computed through fitting as shown in (a) and (b) for all the temperatures. (d) Temperature dependence of four-fold component computed from FFT. Four-fold component and four-fold coefficient display identical temperature dependent behavior.

observe a contribution from the four-fold component, while no pronounced contribution until $\sim$ 7 μm appears above T_{SR}. Below T_{SR}, the four-fold component peaks at length scale around $\sim$ 6 μm and then decreases afterward. Furthermore, we observe a small variation in the length scale where the four-fold component peaks from 5.5 μm to 6 μm between 130 K and 100 K. The two-fold component also appears below T_{SR} and peaks at length scale around $\sim$ 4.5 μm. The two-fold component for $T > T_{SR}$ increases

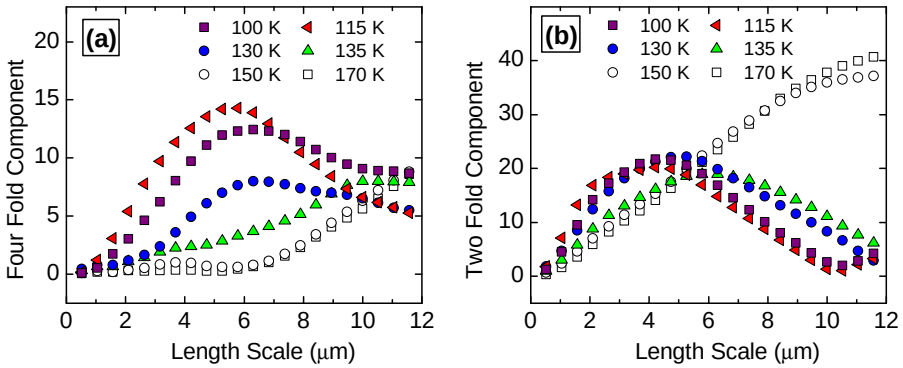

Figure 4.4: (a) and (b) show the length scale dependence of four-fold and two-fold components, respectively. These components are calculated from intensity of autocorrelation and show different response for temperatures below and above T_{SR}.

up to larger length scale which peaks at $\sim$ 12 μm. The length scales corresponding to two-fold and four-fold components represent the average size of magnetic features below T_{SR}. Thus, magnetic features of size $\sim$ 4.5 μm – 6 μm are present in MFM images for $T < T_{SR}$. Our observed magnetic feature size is comparable to previously reported values of 5 μm below T_{SR} using magneto-optical Kerr effect [17]. The magnetic features are the regions between two stripe-like (bluish background) features as shown in Fig. 4.1(c). The stripe-like features also evolve with temperature as their width increases with increase in temperature. For $T > T_{SR}$, the stripe-like features become band-like features. The average width of band-like feature is $\sim$ 12 μm which is displayed by two-fold component in Fig. 4.4(b).

4.3.2 $T > T_{SR}$

The magnetic features of various sizes do not possess any regular shape. Therefore, the size of magnetic features above T_{SR} can not be estimated through either two-fold or four-fold components. However, we estimate the size of magnetic features from the central circular part of autocorrelated images. The average of full width at half maximum (FWHM) is calculated

from different directions as presented in Fig. 4.5 (b), reflects the average size magnetic features. We find feature size of ~ 5 μm for all temperatures above T_{SR}.

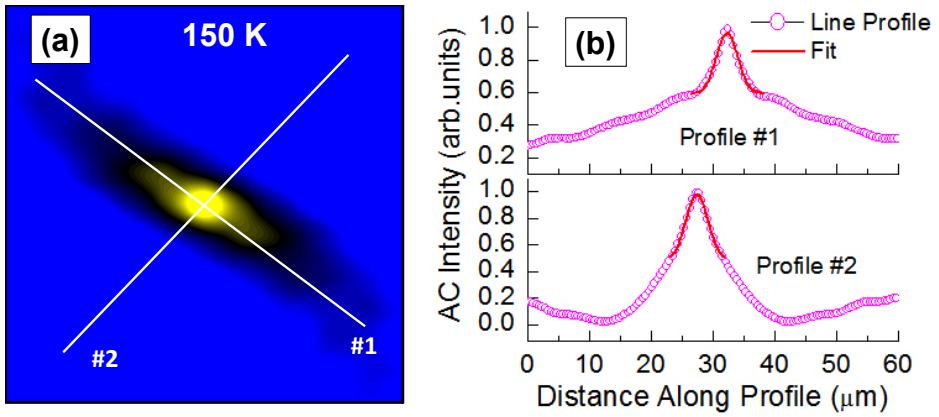

Figure 4.5: (a) Autocorrelation of MFM image at 150 K with two line-profiles through the center. (b) Line-profiles show peak correspond to the central part of autocorrelation. Peaks were fitted to obtain the FWHM.

Chapter 5

Fractal Analysis

5.1 Introduction to fractals

5.1.1 Fundamental concept

Objects of various shapes and sizes can easily be understood and interpreted mathematically through Euclidean geometry, where the characteristic features of regular shapes (i.e., length, area or volume) can easily be defined. For example, in Euclidean geometry, 0, 1, 2 and 3-dimensional space is used to describe dots, lines, areas, and volumes, respectively. The dimension of such objects is expressed in whole integer form and is independent of the size of the measuring scale.

In nature, objects such as trees, mountains, rivers and their banks, clouds, and the human body possess very complex shapes and morphologies. In fact, the shapes of nature are so varied as to deserve being called "geometrically chaotic" [57]. The description of such objects is beyond the scope of Euclidean geometry because approximating such objects in Euclidean geometry produces an inaccurate description. The complexity of such complicated objects was described by Mandelbrot, where he used word "fractal".

A comparison between topological dimension (D_t) and fractal dimension (FD) is described in Fig. 5.1. Both straight and rugged lines have D_t

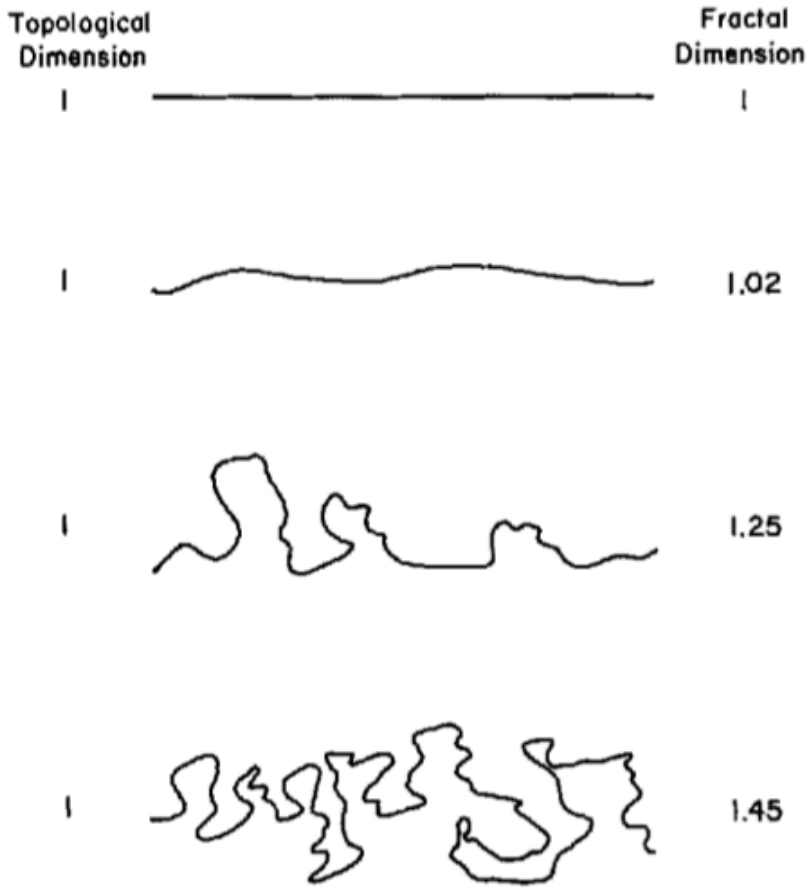

Figure 5.1: A comparison between topological dimension and fractal dimension of a rugged line adapted from Ref. [58].

equal to 1. However, ruggedness of lines is not fully described by the D_t. Mandelbrot proposed that the ruggedness of a line is described by adding fractional number. Therefore, we notice FD exceeds the D_t (i.e., FD $> D_t$). This suggests the dimension of fractals is not equal to the space it resides in. Moreover, one can also notice the complexity in rugged line from FD values.

There are few characteristics that distinguish fractals from Euclidean

shapes. First, FD is relatively new concept where dimension is a fractional quantity unlike the topological dimension. Second, the characteristic properties (length, size, etc...) describing the Euclidean shapes are independent of length of measuring scale. However, FD does change with the size of measuring scale. Third, the Euclidean shape is usually described by mathematical (algebraic) formula, whereas, FD is computed through the slope of log-log plot of measuring scale versus measurement, which results in a non-integer values. Fourth, fractals are self-similar, which means that the object is exactly or approximately a copy of the whole at reduced scale.

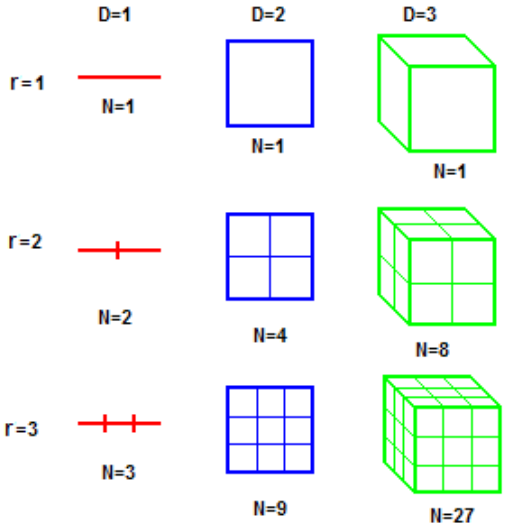

Figure 5.2: The notion of geometry for defining the dimension and scaling in Euclidean shapes. This figure is adapted from Ref. [59].

Self-similarity or scaling factor is a key concept of fractal geometry and is closely connected to the notion of dimension. An example of self-similarity in Euclidean shapes is shown in Fig. 5.2. A one unit long line can be divided into self-similar parts, each of which is scaled down by scaling factor r. The second row of Fig. 5.2 shows the case where r is equal to 2. Similarly, for three self-similar parts, r is 3 and so on. A square (cube) will be divided into 4 (8) and 9 (27) self-similar parts for scaling factors 2 and 3, respectively.

Thus, scaling factor r and number of copies $N(r)$ are related as:

$$N(r) = r^D \tag{5.1}$$

$$D = \frac{\log(N(r))}{\log(r)} \tag{5.2}$$

Thus, from the above equation the dimension D is equal to 1, 2, and 3 for line, square, and cube, respectively.

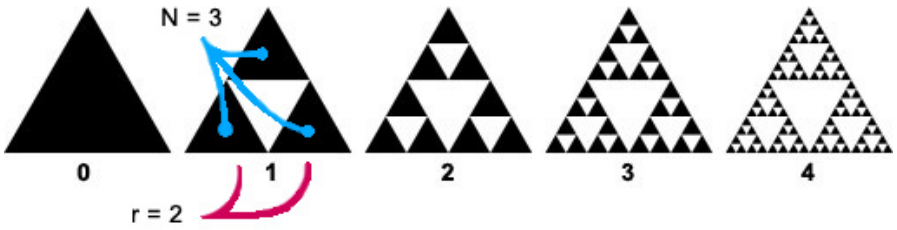

Figure 5.3: Sierpinski Triangle shows fractional dimension. It shows the self-similarity where triangle looks exactly the same whether it is viewed from close or far. This figure is adapted from Ref. [60].

The same method can be implemented to geometric fractal. For instance, the Sierpinski Triangle shown in Fig. 5.3 [60]. The 0 order triangle is scaled down by factor of 2 and three self-similar copies are produced. For scaling factor of 4, nine copies are produced and so on. So in this case:

$$D = \frac{\log(9)}{\log(4)} = 1.58 \tag{5.3}$$

The dimension D of the Sierpinski Triangle is fractional. These examples describe mathematical fractals with true self-similarity, where the object appears identical whether it is viewed from near or far. Each small portion of the structures reproduce the large portion. Such true self-similarity is not present in objects in nature, instead they show statistical self-similarity, which means that shapes have some likeness [61]. It should be noted that

not all self-similar objects are fractal: for example a straight line is self-similar, but not fractal, because its fractal and topological dimensions are equal to 1 [62].

5.1.2 FD computing methods

FD analysis has established itself as a powerful tool to analyze the irregular and complex shapes of different objects. So far, FD analysis has been implemented in almost all the disciplines of sciences and engineering.A multitude of methods have been developed to analyze the fractal features. Since these methods are based on different theoretical bases, one should therefore expect different results for the same feature. There are three main steps that are common in these FD analysis methods:

i. A relationship between measured quantities as a function of various step size (measuring scale) is developed.

ii. A log-log plot of measured quantities versus step sizes is produced.

iii. A linear regression slope of log-log plot is evaluated, which is used to determine the FD.

We briefly discuss several common methods for computing the fractal dimension below.

Divider method

The basic implementation of this method is to walk the divider (yardstick) along the fractal curve and record the number of steps required to cover the fractal curve with a fixed step length [63, 64]. The mathematical formula is:

$$L(G) = FG^{(1-D)}, \tag{5.4}$$

where F is a positive constant, $L(G)$ is the measured length of the line, which depends on step length G. In practice, to get the $L(G)$, there are N values of G. D is the fractal dimension, which is computed from the slope (1-D) of the log-log plot of above equation.

Box-counting method

This is the most popular method for FD analysis introduced by Russel, *et al.* [65]. In this method a binary image is covered with a grid of $N(r)$ boxes of size r. As the size of the box is reduced, the number of boxes increases. The minimum size of the box can become equal to the image resolution. The FD is computed using the formula:

$$FD = -\lim_{r \to 0} \frac{\log(N(r))}{\log(r)} \tag{5.5}$$

The slope of best linear fitting curve of log-log plot gives the FD.

Differential Box-counting method

N. Sarkar and Chaudhuri [66] proposed the differential box counting method where binarization of image is avoided. In this method, an image is gridded into various box size r and $N(r)$ is computed in differential form. A image (M $\times$ M) is scaled down to the different box size (s $\times$ s). For example, an image of 3D space with (x,y) denoting 2D space, are partitioned into different grids (s $\times$ s) and third coordinate (z) denotes the gray levels. The maximum and minimum gray level of image in the $(i,j)^{th}$ grid fall in l^{th} and k^{th} box number, respectively. Then

$$n_r(i,j) = l - k + 1, \tag{5.6}$$

is the contribution of $N(r)$ in $(i,j)^{th}$ grid. The contribution from all the grid cell is

$$N_r = \sum_{ij} n_r(i,j). \tag{5.7}$$

The FD is calculated using the equation 5.5.

Variogram method

This method is based on Gaussian modeling of the image. In this method, the variogram function, which describes how variance in surface height varies with distance, is used for estimating the fractal dimension. Large number

of pairs of points of different spacing along the profile are considered and difference in vertical (z) values is computed. The FD is determined from the log-log plot between the square of the expected difference as a function of distance between the point pair [63], according to

$$\langle [Z_p - Z_q]^2 \rangle \propto (d_{pq})^{4-2D},$$

where D is fractal dimension, Z_p and Z_q are the elevations of points p and q, respectively, while d is distance between p and q.

Power spectrum method

In this method, the power spectrum of the Fourier transform of each image line is evaluated and then all the power spectra are averaged [67]. The FD is determined from the slope. This method is found to be very slow and requires gridded data.

Area-perimeter method

In this method, the FD is computed from the relationship between the perimeter and the area of the features. This method determines the FD of linear features that form the closed loop [68]. The FD of lakes, islands, contour loops, grain boundaries (quartz), and magnetic domains have been computed using the area-perimeter method [69–73]. For fractal grain boundaries, the perimeter P is related to the diameter d or the area A as [63, 70]:

$$P \propto A^{\frac{D}{2}} \propto d^D,$$

where D is FD, which is determined from the slope of linear regression of log-log plot of A and P. The range of fractal dimension is $1 \leq \mathrm{D} \leq 2$ because the measurement is in 2D Euclidean space [71]. The FD obtained represents the collective property of set of features of various sizes. The area-perimeter method is most stable and simple method as compared to variogram and spectral methods [74].

In the next section, we use area-perimeter method to compute the FD of magnetic features. The area-perimeter algorithm is developed in MATLAB and is implemented on binary images.

5.2 Fractal analysis of magnetic features

5.2.1 FD analysis approach

To implement the area-perimeter algorithm, the MFM images were first binarized. A binary images is a digital image that has a series of 0s and 1s. A cutoff value based on pixels intensity is used, where every pixel above the cutoff turns into 1, while pixel values below the cutoff turn into 0. Figure 5.4 shows the binary images as a result of several different cutoff values. It can be seen that for larger cutoffs, there is a greater loss of image information. Therefore, one must be careful while choosing the right cutoff values. Initially, 30 % – 60 % cutoffs with step of 10 % were implemented. It is worth noting that the the chosen cutoff, for example 30 % cutoff means that 30 % pixels of lowest pixel values are discarded. The choice of 50 % cutoff is selected to be a single reasonable cutoff value for all images to obtain the binary image with magnetic features identical to MFM images as shown in Fig 5.6(b).

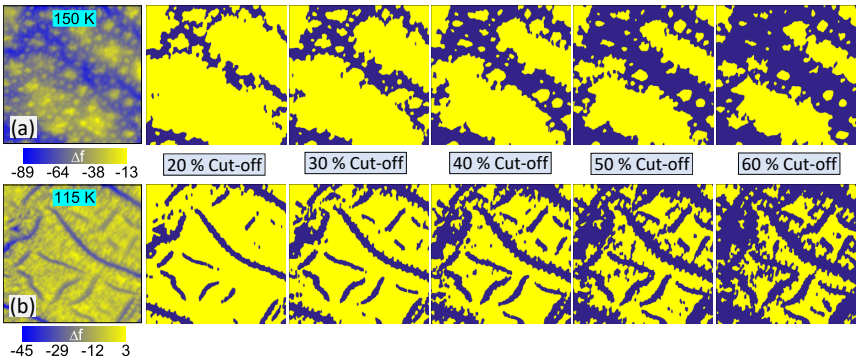

Figure 5.4: Binary images obtained as a result of cutoff values from 20 % to 60 %.

For $T < T_{SR}$, the binary images obtained using initially chosen 50 % cutoff value accurately reproduce the main magnetic features of the MFM images. However, one can notice that the 50 % cutoff values do not look appropriate for $T > T_{SR}$, where binary images contains sizable features. Such

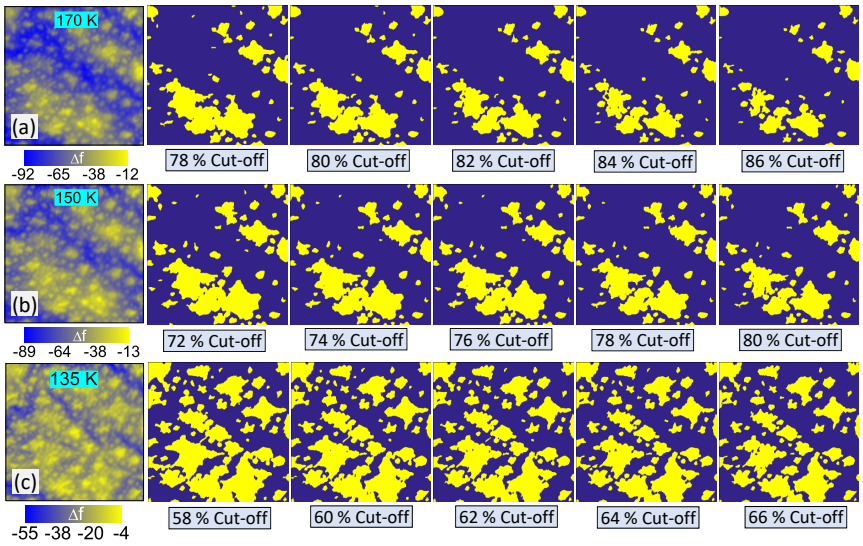

Figure 5.5: Binary images obtained as a result of different range of cutoff values for each image at 170 K, 150 K, and 135 K (T $\geq T_{SR}$).

sizable features do not display the disperse small magnetic features in MFM images. Therefore, these MFM images ($T > T_{SR}$) are binarized for higher cutoff values. Figure 5.5 shows the binary images obtained for higher cutoff values. For 155 K – 170 K, 140 K – 150 K, 135 K, and 100 K – 130 K different range of cutoff values 70 % – 90 % , 60 % – 80 %, 50 % – 70 %, and 40 % – 50 % with step of 1 % were implemented, respectively. Our approach of taking different cutoff values for each image indicates that there is no single cutoff value for the images 170 K – 135 K. Figure 5.6(c) shows binary images for subjectively-determined optimal cutoffs for selected images below and above T_{SR}. For the higher cutoffs, the small magnetic features vanish, however, the main features persist. So in this case, subjectively-determined optimal cutoff value is found to be higher than 50 %, which decreases as temperature decreases. This makes sense because magnetic features are temperature sensitive and modify themselves as temperature decreases. However, magnetic features below T_{SR} do not change much (apparently) as a function of temperature, a single cutoff value about 42 % produces all the binary images

identical to the MFM images.

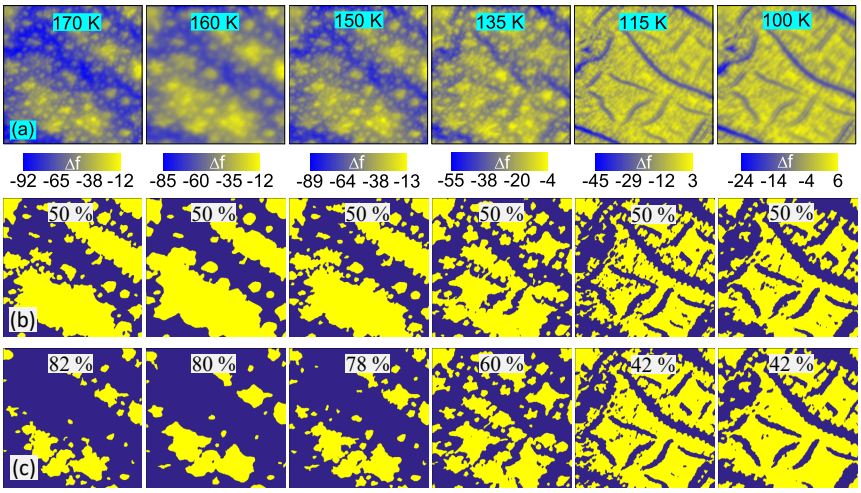

Figure 5.6: Binary images as a result of chosen cutoff values for computing the fractal dimension. (a) MFM images. (b) Binary images obtained for a uniform cutoff value of 50%. (c) Each image is binarized for subjectively-determined optimal cutoff values for T $\geq$ 135 K (T_{SR}) which is larger than 50 % cutoff value, while images from 130 K to 100 K are binarized for 42 % cutoff values.

After obtaining the binary images, we implement the area-perimeter (AP) algorithm, which generates several areas and corresponding perimeter values. Then log-log plot of area versus perimeter is produced. The data points are fitted through linear regression method and FD is computed from the slope of the fitted line.

5.2.2 Fractal results

Figure 5.7 shows the log-log plots of area versus perimeter of magnetic features at different temperatures. The fractal dimension (FD) is related to the slope of fitted line by FD = 2×slope. We expect that the FD should vary with temperature, since magnetic features change with temperature.

The computed FD as a function of temperature are shown in Fig. 5.8. Since fractal nature is related to the nonlinear, irregular, and complex struc-

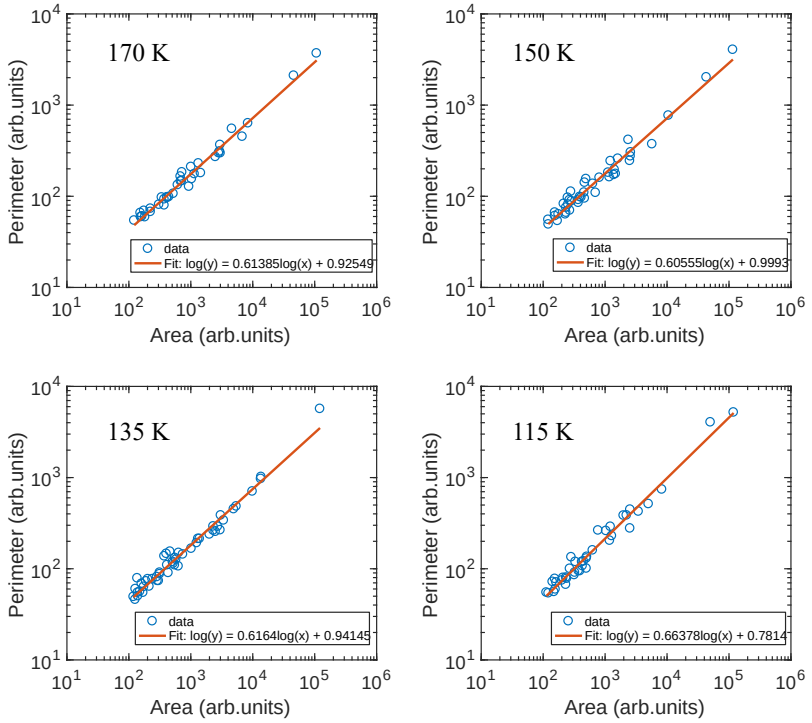

Figure 5.7: Log-log plots of perimeter versus area of magnetic features from the binary images. Linear regression is perform to fit the data. The slope of fitted line is used to compute the fractal dimension using equation FD = 2×slope.

tures, therefore, FD is a useful parameter to describe them quantitatively. The computed FD describes the degree of complexity in boundary structure of the magnetic features. The growing behavior of the magnetic features with decrease in temperature can be understood from the structure of the boundaries using the FD information.

The computed FD are found to be greater than 1 for all the images, which means that the boundaries of magnetic features are not smooth. The computed values of FD indicate that the boundaries possess complexity due to ruggedness in their structure. We also notice an increase in the FD below spin reorientation transition (T = 135 K) as shown in Fig. 5.8(a). An

abrupt increase in FD proves the role of spin reorientation transition on the magnetic feature geometry. The higher values of FD below T_{SR} indicates that magnetic features in this new magnetic phase not only produce new type of magnetic features (discussed in Chapter 4), but also possess higher complexity. The temperature dependent behavior also indicates the lack of consistency in FD values from one temperature to another temperature which is quite obvious for temperatures $T > T_{SR}$ (135 K). The FD for images at 170 K, 155 K and 150 K are higher than rest of the images in 170 K – 140 K region. This inconsistency might be related to the experimental factor during the MFM scan. This is evident in images taken at 150 K and 160 K as shown in Fig. 5.6(a), where image at 160 K looks slightly blurred compared to 170 K and 150 K images.

Figure 5.8(b) shows very similar FD behavior as a function of temperature. Although, the choice of higher cutoffs cause the small magnetic features to disappear and left the large magnetic feature. However, individual cutoffs for each image does not influence the overall FD of the magnetic features. Here, we also notice that FD for 150 K and 155 K are also higher than images at other temperatures above T_{SR} similar to Fig. 5.6(a). This rules out the possible effect of chosen cutoff values on the computed FD values. It should be noted that the computed FD do not represent the rugged nature of the boundaries of a single magnetic feature, rather gives us an average of all the features in the image.

Figure 5.8 (c) shows the effect of subjectively-determined optimal cutoff values on the computed FD. We can see that no matter what reasonable cutoff values we choose, the temperature dependent behavior of computed FD stays the same. Moreover, fractal values of binary images obtained at different cutoffs stay very close to each other. The average FD changes from 1.18 $\pm$ 0.04 to 1.28 $\pm$ 0.04 for the magnetic features observed above and below spin reorientation transition, respectively for 50 % cutoff values (Fig. 5.8(a)). Similarly, binary images produced from subjectively-determined optimal cutoffs, FD (average values) changes from 1.17 $\pm$ 0.05 to 1.29 $\pm$ 0.04 for magnetic features observed above and below T_{SR}.

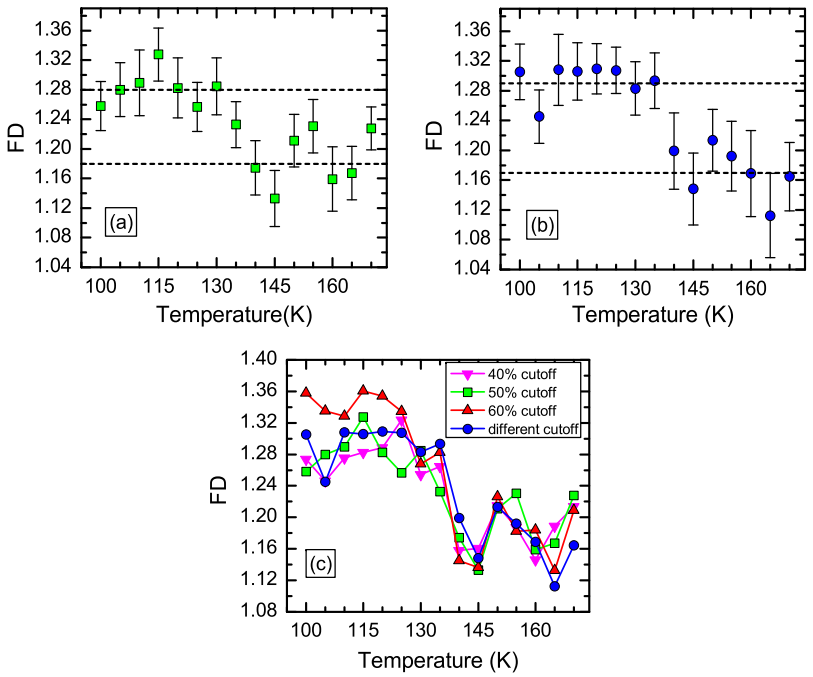

Figure 5.8: Fractal dimension (FD) as a function of temperature. The error bars are obtained from slope uncertainty. (a) FD of the binary images obtained for uniform cutoff value of 50 %. (b) FD of images binarized for subjectively-determined optimal cutoff values. Dashed lines show average FD for $T > T_{SR}$ and $T < T_{SR}$. (c) A comparison of FD for all binary images produced for different cutoff values.

Chapter 6

Conclusions

We studied the magnetic features of $Nd_2Fe_{14}B$ single crystal from MFM images obtained at various temperatures (170 K – 100 K) including the spin reorientation transition temperature (T_{SR} = 135 K). A new type of magnetic features emerge below T_{SR}, where four magnetization directions form an easy-cone of magnetization. The magnetic features of irregular shapes observed above T_{SR}, which transformed into distorted rectangular magnetic features below T_{SR}.

The size of magnetic features below T_{SR} is determined from the autocorrelation of MFM images. We noticed the presence of two-fold and four-fold anisotropies in the autocorrelated images. Both two-fold and four-fold anisotropy components are found to be length scale dependent. The two-fold and four-fold anisotropy components peak around length scale $\sim$ 6 μm and $\sim$ 4.5 μm, respectively, and are related to the size of magnetic features (4.5 μm – 6 μm) below T_{SR}. Above T_{SR}, no contribution from the four-fold component of anisotropy is seen in the autocorrelation images, while the two-fold component was attributed to the band-like structure in MFM images. Thus, anisotropy components did not incorporate the size of magnetic features above T_{SR}. The average magnetic feature size $\sim$ 5 μm is estimated above spin reorientation temperature from the FWHM of the central part of the autocorrelated images.

The geometry of magnetic features is studied from the fractal dimension

(FD). The complexity of magnetic features is quantified from the FD values. The area-perimeter method is used to compute the FD. To implement the area-perimeter algorithm, MFM images were first binarized. FD shows a temperature dependent behavior and increased from 1.17 $\pm$ 0.05 to 1.29 $\pm$ 0.04. The higher value of FD revealed the more complex nature of magnetic features below T_{SR} compared to magnetic features observed above T_{SR}. Furthermore, different cutoffs for binarization did not alter the FD value significantly.

Further investigation can be carried out to study the magnetic features deeply and their correlation below and above T_{SR}. MFM images over a few microns area might be useful to study the domain walls, their evaluation through spin reorientation transition, and the fractal nature of magnetic domains.

Bibliography

[1] J.M.D. Coey. Permanent magnet applications. *Journal of Magnetism and Magnetic Materials*, 248(3):441–456, 2002.

[2] M. Honshima and K. Ohashi. High-energy NdFeB magnets and their applications. *Journal of Materials Engineering and Performance*, 3(2):218–222, 1994.

[3] Rob H.J. Fastenau and Evert J. van Loenen. Applications of rare earth permanent magnets. *Journal of Magnetism and Magnetic Materials*, 157-158:1–6, 1996.

[4] Tsung-Shune Chin. Permanent magnet films for applications in micro-electromechanical systems. *Journal of Magnetism and Magnetic Materials*, 209(1-3):75–79, 2000.

[5] N. M. Dempsey, A. Walther, F. May, D. Givord, K. Khlopkov, and O. Gutfleisch. High performance hard magnetic NdFeB thick films for integration into micro-electro-mechanical systems. *Applied Physics Letters*, 90(9):092509, 2007.

[6] A. Walther, K. Khlopkov, O. Gutfleisch, D. Givord, and N.M. Dempsey. Evolution of magnetic and microstructural properties of thick sputtered NdFeB films with processing temperature. *Journal of Magnetism and Magnetic Materials*, 316(2):174–176, 2007.

[7] G. Bai, R.W. Gao, Y. Sun, G.B. Han, and B. Wang. Study of high-coercivity sintered NdFeB magnets. *Journal of Magnetism and Magnetic Materials*, 308(1):20–23, 2007.

[8] Oliver Gutfleisch. Controlling the properties of high energy density permanent magnetic materials by different processing routes. *Journal of Physics D: Applied Physics*, 33(17):R157–R172, 2000.

[9] J. F. Herbst. R2Fe14B materials: Intrinsic properties and technological aspects. *Reviews of Modern Physics*, 63(4):819–898, 1991.

[10] D W Scott, B M Ma, Y L Liang, and C O Bounds. Microstructural control of NdFeB cast ingots for achieving 50 MGOe sintered magnets. *Journal of Applied Physics*, 79(8):4830, 1996.

[11] M. Sagawa, S. Fujimura, H. Yamamoto, Y. Matsuura, and S. Hirosawa. Magnetic properties of rareearthironboron permanent magnet materials. *Journal of Applied Physics*, 57(8):4094–4096, 1985.

[12] J. Pastushenkov, A. Forkl, and H. Kronmüller. Magnetic domain structure of sintered Fe-Nd-B type permanent magnets and magnetostatic grain interaction. *Journal of Magnetism and Magnetic Materials*, 101(1-3):363–366, 1991.

[13] J. D. Livingston. Magnetic domains in sintered FeNdB magnets. *Journal of Applied Physics*, 57(8):4137–4139, 1985.

[14] K. Tokuhara, Y. Ohtsu, F. Ono, O. Yamada, M. Sagawa, and Y. Matsuura. Magnetization and torque measurements on Nd2Fe14B single crystals. *Solid State Communications*, 56(4):333–336, 1985.

[15] D. Givord, H.S. Li, and R. Perrier de la Bâthie. Magnetic properties of Y2Fe14B and Nd2Fe14B single crystals. *Solid State Communications*, 51(11):857–860, 1984.

[16] Yu.G. Pastushenkov, A. Forkl, and H. Kronmüller. Temperature dependence of the domain structure in Fe14Nd2B single crystals during the spin-reorientation transition. *Journal of Magnetism and Magnetic Materials*, 174(3):278–288, 1997.

[17] Yu.G. Pastushenkov, K.P. Skokov, N.P. Suponev, and D. Stakhovski. Low-temperature magnetization distribution and magnetization reversal in FeNdB permanent magnets. *Journal of Magnetism and Magnetic Materials*, 290-291:644–646, 2005.

[18] Yu. G Pastushenkov. Some features of magnetic domain structure reorganization during spin-reorientation phase transitions of the first and second order. *Bulletin of the Russian Academy of Sciences: Physics*, 74(10):1423–1425, 2010.

[19] L H Lewis, J.-Y. Wang, and P Canfield. Magnetic domains of single-crystal Nd2Fe14B imaged by unmodified scanning electron microscopy. *Journal of Applied Physics*, 83(11):6843–6845, 1998.

[20] Yimei Zhu and M. R. McCartney. Magnetic-domain structure of Nd2Fe14B permanent magnets. *Journal of Applied Physics*, 84(6):3267–3272, 1998.

[21] Jy Wang, Lh Lewis, Do Welch, and Paul Canfield. Magnetic Domain Imaging of Nd2Fe14B Single Crystals With Unmodified Scanning Electron Microscopy. *Materials Characterization*, 41(5):201–209, 1998.

[22] Kanta Ono, Tohru Araki, Masao Yano, Noritaka Miyamoto, Tetsuya Shoji, Akira Kato, Akira Manabe, Hiroshi Nozaki, Yuji Kaneko, and Jörg Raabe. Element-Specific Magnetic Domain Imaging of (Nd, Dy)-Fe-B Sintered Magnets Using Scanning Transmission X-Ray Microscopy. *IEEE Transactions on Magnetics*, 47(10):2672–2675, 2011.

[23] Volker Neu, Steffen Melcher, Ullrich Hannemann, Sebastian Fähler, and Ludwig Schultz. Growth, microstructure, and magnetic properties of highly textured and highly coercive Nd-Fe-B films. *Physical Review B*, 70(14):144418, 2004.

[24] M. Al-Khafaji, W. M. Rainforth, M. R. J. Gibbs, J. E. L. Bishop, and H. A. Davies. The origin and interpretation of fine scale magnetic contrast in magnetic force microscopy: A study using single-crystal Nd-FeB and a range of magnetic force microscopy tips. *Journal of Applied Physics*, 83(11):6411, 1998.

[25] Lunan Huang, Valentin Taufour, T. N. Lamichhane, Benjamin Schrunk, Sergei L. Bud'ko, P. C. Canfield, and Adam Kaminski. Imaging the magnetic nanodomains in Nd2Fe14B. *Physical Review B*, 93(9):094408, 2015.

[26] A. Kreyssig, R. Prozorov, C. D. Dewhurst, P. C. Canfield, R. W. McCallum, and A. I. Goldman. Probing Fractal Magnetic Domains on Multiple Length Scales in Nd2Fe14B. *Physical Review Letters*, 102(4):047204, 2009.

[27] L. Folks, R. Street, and R. C. Woodward. Domain structures of die-upset melt-spun NdFeB. *Applied Physics Letters*, 65(7):910, 1994.

[28] Witold Szmaja. Investigations of the domain structure of anisotropic sintered NdFeB-based permanent magnets. *Journal of Magnetism and Magnetic Materials*, 301(2):546–561, 2006.

[29] H. Lemke, T. Goddenhenrich, C. Heiden, and G. Thomas. Thin Nd-Fe-B films analyzed by Lorentz and magnetic force microscopy. *IEEE Transactions on Magnetics*, 33(5):3865–3867, 1997.

[30] Xiaoxi Liu, Shinsaku Isomura, and Akimitsu Morisako. Magnetic vortex core for high resolution magnetic force microscopy. In *2013 13th IEEE International Conference on Nanotechnology (IEEE-NANO 2013)*, pages 794–797. IEEE, 2013.

[31] M. Precner, J. Fedor, J. Tóbik, J. Šoltýs, and V. Cambel. High Resolution Tips for Switching Magnetization MFM. *Acta Physica Polonica A*, 126(1):386–387, 2014.

[32] J F Herbst, J J Croat, F E Pinkerton, and W B Yelon. Relationships between crystal structure and magnetic properties in Nd2Fe14B. *Physical Review B*, 29(7):4176–4178, 1984.

[33] D. Givord, H.S. Li, and J.M. Moreau. Magnetic properties and crystal structure of Nd2Fe14B. *Solid State Communications*, 50(6):497–499, 1984.

[34] C. B. Shoemaker, D. P. Shoemaker, and R. Fruchart. The structure of a new magnetic phase related to the sigma phase: iron neodymium boride Nd2Fe14B. *Acta Crystallographica Section C Crystal Structure Communications*, 40(10):1665–1668, 1984.

[35] Nedko Drebov, Alberto Martinez-Limia, Lothar Kunz, Adrien Gola, Takashi Shigematsu, Thomas Eckl, Peter Gumbsch, and Christian Elsässer. Ab initio screening methodology applied to the search for new permanent magnetic materials. *New Journal of Physics*, 15(12):125023, 2013.

[36] H R Kirchmayr. Permanent magnets and hard magnetic materials. *Journal of Physics D: Applied Physics*, 29(11):2763–2778, 1996.

[37] Yoshichika Otani, Hideki Miyajima, and Sshin Chikazumi. Magnetocrystalline anisotropy in NdFeB magnet. *Journal of Applied Physics*, 61(8):3436–3438, 1987.

[38] O. Yamada, H. Tokuhara, F. Ono, M. Sagawa, and Y. Matsuura. Magnetocrystalline anisotropy in Nd2Fe14B intermetallic compound. *Journal of Magnetism and Magnetic Materials*, 54-57(15):585–586, 1986.

[39] Masato Sagawa, Satoshi Hirosawa, Hitoshi Yamamoto, Setsuo Fujimura, and Yutaka Matsuura. NdFeB Permanent Magnet Materials. *Japanese Journal of Applied Physics*, 26(Part 1, No. 6):785–800, 1987.

[40] Motohiko Yamada, Hiroaki Kato, Hisao Yamamoto, and Yasuaki Nakagawa. Crystal-field analysis of the magnetization process in a series of Nd2Fe14B-type compounds. *Physical Review B*, 38(1):620–633, 1988.

[41] Jesús Chaboy, Luis M. García, Fernando Bartolomé, Augusto Marcelli, Giannantonio Cibin, Hiroshi Maruyama, Stefania Pizzini, Andrei Rogalev, Jeroen B. Goedkoop, and José Goulon. X-ray magnetic-circular-dichroism probe of a noncollinear magnetic arrangement below the spin reorientation transition in Nd2Fe14B. *Physical Review B*, 57(14):8424–8429, 1998.

[42] Hideya Onodera, Akira Fujita, Hisao Yamamoto, Masato Sagawa, and Satoshi Hirosawa. Mössbauer study of the intermetallic compound Nd2Fe14B. I. interpretation of complex spectrum. *Journal of Magnetism and Magnetic Materials*, 68(1):6–14, 1987.

[43] I Nowik, K Muraleedharan, G Wortmann, B Perscheid, G Kaindl, and N.C Koon. Spin reorientation transition in Nd2Fe14B studied by 145Nd-Mössbauer spectroscopy. *Solid State Communications*, 76(8):967–970, 1990.

[44] Raja K. Mishra and Robert W. Lee. Microstructure, domain walls, and magnetization reversal in hotpressed NdFeB magnets. *Applied Physics Letters*, 48(11):733–735, 1986.

[45] Oscar Iglesias-Freire, Jeffrey R. Bates, Yoichi Miyahara, Agustina Asenjo, and Peter H. Grutter. Tip-induced artifacts in magnetic force microscopy images. *Applied Physics Letters*, 102(2):022417, 2013.

[46] Y. Martin and H. K. Wickramasinghe. Magnetic imaging by force microscopy" with 1000 Å resolution. *Applied Physics Letters*, 50(20):1455–1457, 1987.

[47] J. J. Sáenz, N. García, P. Grütter, E. Meyer, H. Heinzelmann, R. Wiesendanger, L. Rosenthaler, H. R. Hidber, and H.J. Güntherodt.

Observation of magnetic forces by the atomic force microscope. *Journal of Applied Physics*, 62(10):4293–4295, 1987.

[48] G. Binnig, C. F. Quate, and Ch. Gerber. Atomic Force Microscope. *Physical Review Letters*, 56(9):930–933, 1986.

[49] M.A. Al-Khafaji, W.M. Rainforth, M.R.J. Gibbs, J.E.L. Bishop, and H.A. Davies. The effect of tip type and scan height on magnetic domain images obtained by MFM. *IEEE Transactions on Magnetics*, 32(5):4138–4140, 1996.

[50] M. A. Al-Khafaji, D. G. R. Jones, W. M. Rainforth, M. R. J. Gibbs, H. A. Davies, and I. R. Harris. Magnetic force imaging of domain structures for a (Pr/Nd)FeB alloy. *Journal of Applied Physics*, 83(5):2715, 1998.

[51] Steffen Porthun, Leon Abelmann, and Cock Lodder. Magnetic force microscopy of thin film media for high density magnetic recording. *Journal of Magnetism and Magnetic Materials*, 182(1-2):238–273, 1998.

[52] U. Hartmann. MAGNETIC FORCE MICROSCOPY. *Annual Review of Materials Science*, 29(1):53–87, 1999.

[53] A Hendrych, R Kubínek, and A V Zhukov. The magnetic force microscopy and its capability for nano- magnetic studies - The short compendium. *Modern Research and Educational Topics in Microscopy*, pages 805–811, 2007.

[54] Leon Abelmann, A. van den Bos, and Cock Lodder. Magnetic Force Microscopy Towards Higher Resolution. In *Magnetic Microscopy of Nanostructures*, pages 253–283. 2005.

[55] Yi Liu, D J Sellmyer, and D Shindo. *Handbook of Advanced Magnetic Materials: Vol 1. Nanostructural Effects. Vol 2. Characterization and Simulation. Vol 3. Fabrication and Processing. Vol 4. Properties and Applications.* Springer Science & Business Media, 2008.

[56] Claire Robertson. Theory and practical recommendations for autocorrelation-based image correlation spectroscopy. *Journal of Biomedical Optics*, 17(8):080801, 2012.

[57] B. B. Mandelbrot and A. Blumen. Fractal Geometry: What is it, and What Does it do? *Proceedings of the Royal Society A: Mathematical, Physical and Engineering Sciences*, 423(1864):3–16, 1989.

[58] Brian H. Kaye. Applications of Recent Advances in Fineparticle Characterization to mineral processing. *Particle & Particle Systems Characterization*, 2(1-4):91–97, 1985.

[59] https://en.wikipedia.org/wiki/Fractal_dimension.

[60] http://fractalfoundation.org/OFC/OFC-10-3.html.

[61] B. Mandelbrot. How Long Is the Coast of Britain? Statistical Self-Similarity and Fractional Dimension. *Science*, 156(3775):636–638, 1967.

[62] D.E. Roach and A.D. Fowler. Dimensionality analysis of patterns: fractal measurements. *Computers & Geosciences*, 19(6):849–869, 1993.

[63] Brian Klinkenberg. A review of methods used to determine the fractal dimension of linear features. *Mathematical Geology*, 26(1):23–46, 1994.

[64] Robert Andrle. Estimating fractal dimension with the divider method in geomorphology. *Geomorphology*, 5(1-2):131–141, 1992.

[65] David A. Russell, James D. Hanson, and Edward Ott. Dimension of Strange Attractors. *Physical Review Letters*, 45(14):1175–1178, 1980.

[66] Nirupam Sarkar and B.B. Chaudhuri. An efficient differential box-counting approach to compute fractal dimension of image. *IEEE Transactions on Systems, Man, and Cybernetics*, 24(1):115–120, 1994.

[67] R. Lopes and N. Betrouni. Fractal and multifractal analysis: A review. *Medical Image Analysis*, 13(4):634–649, 2009.

[68] B B Mandelbrot. Stochastic models for the Earth's relief, the shape and the fractal dimension of the coastlines, and the number-area rule for islands. *Proceedings of the National Academy of Sciences*, 72(10):3825–3828, 1975.

[69] S. Lovejoy. Area-Perimeter Relation for Rain and Cloud Areas. *Science*, 216(4542):185–187, 1982.

[70] Miki Takahashi, Hiroyuki Nagahama, Toshiaki Masuda, and Akio Fujimura. Fractal analysis of experimentally, dynamically recrystallized quartz grains and its possible application as a strain rate meter. *Journal of Structural Geology*, 20(2-3):269–275, 1998.

[71] Miki Takahashi and Hiroyuki Nagahama. The sections' fractal dimension of grain boundary. *Applied Surface Science*, 182(3-4):297–301, 2001.

[72] Dong Hyun Kim, Yoon Chul Cho, Sug Bong Choe, and Sung Chul Shin. Correlation between fractal dimension and reversal behavior of magnetic domain in Co/Pd nanomultilayers. *Applied Physics Letters*, 82(21):3698–3700, 2003.

[73] Odile Bezencenet, Daniel Bonamy, Rachid Belkhou, Philippe Ohresser, and Antoine Barbier. Origin and Tailoring of the Antiferromagnetic Domain Structure in alph-Fe2O3 thin films unraveled by statistical analysis of dichroic spectro-microscopy (X-PEEM) images. *Physical Review Letters*, 106(10):107201, 2011.

[74] M. Sakellariou, B. Nakos, and C. Mitsakaki. On the fractal character of rock surfaces. *International Journal of Rock Mechanics and Mining Sciences & Geomechanics Abstracts*, 28(6):527–533, 1991.